Chapter 15
Dual-Modality Preclinical PET/MRI Instrumentation

David Schlyer and Bosky Ravindranath

1 Introduction

Multimodality imaging using positron emission tomography (PET) and Magnetic resonance imaging (MRI) is emerging as an extremely valuable tool for investigating disease and physiological processes in small animal models. MRI has high spatial resolution but low sensitivity for detecting low abundance molecules and PET has very high sensitivity for the detection of radiotracers but relatively poor spatial resolution. The combination of these two molecular imaging techniques offers synergistic advantages over either modality alone. A fused anatomical and functional image affords complementary information that clearly improves our understanding. Images acquired simultaneously offer distinct advantages over sequential image acquisition since this gives "perfect" coregistration and observing the same process from two different vantage points can ensure the correlation of information that is impossible in separate experiments.

PET/CT has become the standard for clinical imaging studies because CT also gives anatomical detail not possible with PET. However, PET/MRI is better in several respects as a diagnostic tool than PET/CT, and even more so in pre-clinical, small-animal studies. In the simplest application, using MRI data to detect and correct for motion during a PET scan, and making optimum use of dynamic data is likely to lead to better, more detailed images. The study of tumor uptake and dynamics with dual-labeled, functionalized nanoparticle contrast agents [1], and simultaneous PET and fMRI monitoring of brain activity are just two examples of the possibilities with this dual-modality system. PET employs radiotracers that target

D. Schlyer (✉)
Biosciences Department, Brookhaven National Laboratory, Upton, NY, USA
e-mail: schlyer@bnl.gov

B. Ravindranath
Biomedical Engineering Department, SUNY Stony Brook, Stony Brook, NY, USA
e-mail: bosky@bnl.gov

H. Zaidi (ed.), *Molecular Imaging of Small Animals: Instrumentation and Applications*,
DOI 10.1007/978-1-4939-0894-3_15,

specific sites or molecules with a sensitivity many orders-of-magnitude greater than is possible with current MRI techniques, but PET cannot distinguish the molecular species to which the radioactive atom is attached. Combining PET radiotracers with magnetic resonance spectroscopy (MRS) using C-13 labeled tracers could significantly improve our insight into molecular processes occurring in the body [2]. Some additional advantages are listed below:

- Radiation dose is reduced. MRI does not contribute to the patient's radiation dose whereas the dose from a CT scan is significant.
- Excellent spatial registration is obtained between the MRI and PET images. This ability is particularly important for organs and tissues whose position and shape can shift even between temporally proximal scans.
- Soft-tissue contrast is enhanced, and tissue boundaries are more clearly delineated than is possible with CT. This may support reliable partial-volume correction of PET data that can be very important for quantitative clinical data.
- Accurate temporal registration between the MRI and PET scans allows the determination of pharmacokinetics and pharmacodynamics. The MRI data also could be used to obtain blood flows and to correct for the effects of blood-vessel partial volume, effects that are inherent in the PET data sets, potentially enabling accurate measurement of input functions from this data without requiring arterial sampling.
- The magnetic field of the MRI may slightly improve the PET spatial resolution for high energy positron emitters, as is the case for some non-traditional PET radionuclides being used in preclinical studies.

Several approaches have been explored in the pursuit of the goal of simultaneous PET and MRI. There has been significant progress in identifying PET scintillators with magnetic properties [3] which are compatible with MRI. PET/MRI tomographs have been designed that use optical fibers to transmit the scintillation light from the crystal out of the magnetic field of the MRI to photomultiplier tubes (PMTs) [4–9]. Several groups favor a design that replaces the PMTs in the PET tomograph with magnetic field-insensitive avalanche photodiodes (APD) [10–16]. Since one issue in running PET and MRI simultaneously is the potential for the two modalities to interfere, there has been some effort to design shielded PET electronics to avoid electromagnetic interference [17]. However, several technical challenges remain that must be met to reduce or eliminate such interference. We describe the history of the development of this instrumentation, and its current state-of-the art in the following sections.

2 Instrumentation Development

2.1 PET Using PMTs and Optical Fiber Technology

Early commercial PET scanners for human and animal imaging were built on the concept of directly coupling a scintillator, such as Bismuth Germanate (BGO), to a PMT. The earliest commercially available animal PET scanner, the CTI/Siemens

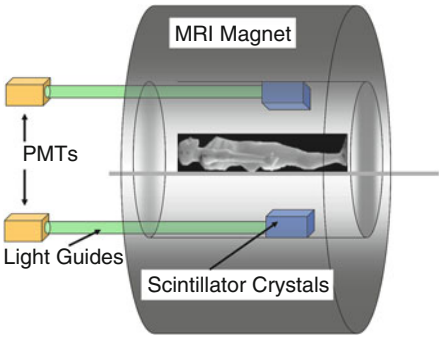

Fig. 15.1 Schematic of combined PET and MRI scanner where light from scintillator blocks inside the MRI scanner is guided to PMTs placed in a low magnetic field via light guides, as described by Hammer [19]

Animal Tomograph—model 713 [18] was built on this concept. It utilized Anger type logic for locating the event position and had a reconstructed transaxial radial spatial-resolution ranging from 3.8 mm full-width-at-half-maximum (FWHM) at the center of the scanner, to 6.7 mm FWHM at a radius of 12 cm; the scanner's tangential resolution was consistent at 3.8 mm FWHM.

The prospect for simultaneous PET and MRI imaging has intrigued researchers since the early 1980s. Complimentary imaging information offered by the two modalities and the improvement in the PET's spatial resolution when using high-energy isotopes in strong magnetic fields engendered new approaches for combining these two imaging modalities. The most logical approach towards integrating them was to develop an MRI-compatible PET insert; the first such device was patented by Hammer in 1990 [19]. The then-available scintillator-PMT combination for PET scanners was not MRI-compatible due to the sensitivity of the PMT to magnetic fields. The presence of PMTs also made the magnetic field inhomogeneous, so distorting the MRI image. Researchers recognized that the key to making the two imaging modalities compatible was to position PMTs in a region of low magnetic-field strength where they could function normally and not disturb the homogeneity of the MRI's magnetic field. Guiding the optical photons from the scintillator blocks to the PMTs via light guides accomplished this aim (Fig. 15.1). The portion of the PET detector that is positioned in the MRI's field-of-view is free of ferromagnetic material, so minimizing inhomogeneities and susceptibility artifacts in the MRI image.

Such a design was implemented in a prototype system with two NaI(T1) scintillation crystals placed inside a 5 T magnet and coupled to the PMTs via a cylindrical Lucite rod [4]. A measurement of the point-spread function of a Ge-68 source inside the 5 T magnet showed a FWHM of 1.64 mm, while outside the magnet the FWHM was 2.19 mm, suggesting an improvement in resolution from a reduction in the range of the positrons perpendicular to the 5 T field.

To image and quantify a radiotracer's concentration in the organs of small animals, a small animal PET must have high resolution. Resolution using block detector technology is limited by the size of the individual crystals in the block detector array, mispositioning of events by the light-sharing technology used and the inability to identify interactions undergoing multiple scatter within a block. BGO scintillators was chosen for its high density, but had the limitations of being difficult to

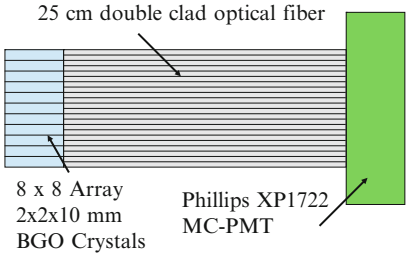

Fig. 15.2 Schematic of array of BGO crystals with one-to-one coupling with multi-channel PMT via optical fibers used in the microPET module

saw into finer crystals and having low light output making positioning of events using Anger logic for larger array of finer crystals difficult [20].

Cherry et al. [21, 22] developed an approach to work around this problem. Instead of using saw cuts to divide a block of scintillator into array of smaller crystals, finer individual crystal elements were stacked together and coupled on a one-to-one basis with an individual pixel of a multi-channel photomultiplier tube through optical fibers. This approach overcomes the size limitation of individual crystal pixels, thereby increasing the intrinsic resolution possible, reducing errors in event positioning, eliminating light-sharing, and correctly identifying and rejecting scattered events. Figure 15.2 is a schematic of such a detector array, which is the building block of the Concord microPET® high-resolution small animal imaging system.

As Fig. 15.2 shows, such an arrangement of scintillators and PMT lends itself to simultaneous PET/MRI imaging, similar to the design proposed by Hammer. The scintillator array is placed inside the MRI's bore and connected on a one-to-one basis by optical fibers to the PMT placed in a low magnetic field area well outside the magnet. Shao and Cherry utilized this design as the McPET (MRI Compatible PET) system [7]. This scanner produced the first simultaneous PET/MRI images.

The McPET I system consisted of a ring of forty eight $2\times2\times10$ mm^3 Lutetium Oxyorthosilicate (LSO) crystals of inner diameter 38 mm, connected via 2 mm diameter, 4 m long double clad optical fibers to three multi channel PMTs (MC-PMT). Each 2×2 mm^2 LSO crystal face was coupled to each individual element of the MC-PMT. The crystals were arranged such that their 10 mm side formed the scanner's axial length. The crystal ring of McPET I was placed inside the radio frequency receiver coil of a 0.2 T open magnet MRI. The MC-PMTs were positioned at 3 m from the center of the MRI's bore, where the magnetic field was less than 0.1 mT and the MC-PMTs could be operated properly (B less than or equal to 10 mT). A steel box shielded the MC-PMTs and their associated readout electronics from ambient light, magnetic fields, and radio frequencies. Figure 15.3 is an image of a newer version of the McPET system, showing its positioning in the MRI machine.

McPET I had a reconstructed spatial resolution of 2.1 mm at the center, an energy resolution of 41 % at 511 keV, and a coincidence timing resolution of 20 ns FWHM.

A second prototype (McPET II) was fabricated [8] consisting of seventy two $2\times2\times5$ mm^3 LSO crystals arranged in a ring with an inner diameter of 54 mm. The crystals of McPET II are arranged such that their 5 mm length forms the thickness of the scanner in the radial direction. This arrangement increases the system's stopping efficiency from 14 % in the McPET I to 34 % in the McPET II. McPET II has

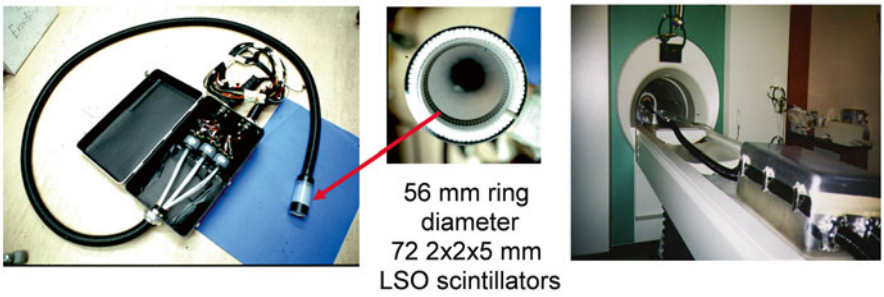

Fig. 15.3 *Left*: picture of the McPET system's detector module. *Right*: detector system installed inside the MRI magnet (Pictures courtesy of Simon Cherry)

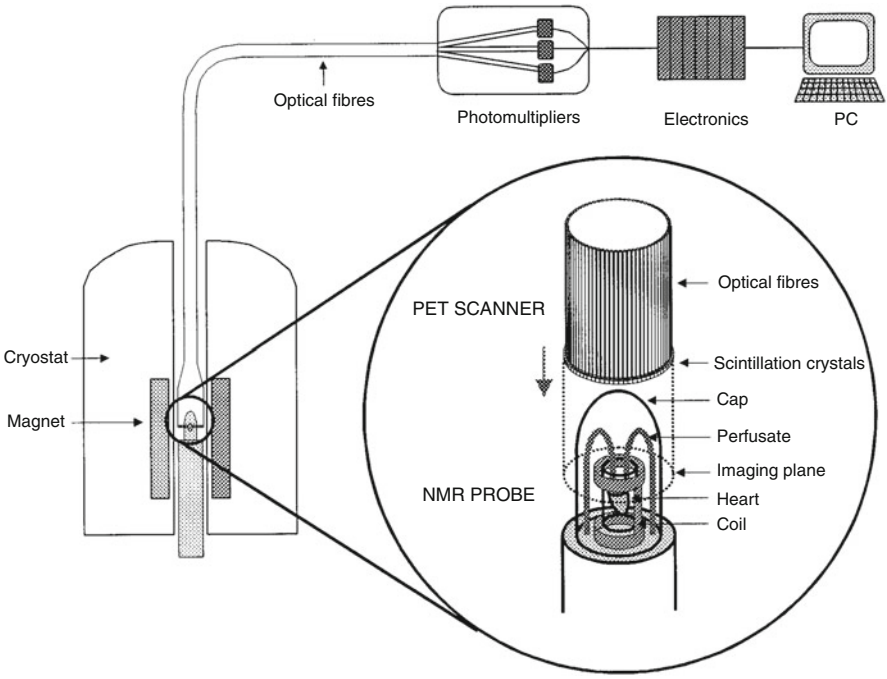

Fig. 15.4 Arrangement of McPET II inside the Bruker 9.4 T spectrometer with a custom-designed NMR probe in place. Reprinted with permission from Garlick et al. [23]

an energy resolution of 45 % and a coincidence timing resolution of 26 ns, both lower than McPET I due to light loss from the optical fibers being coupled to the crystal's side face (2×5 mm).

Along with simultaneous PET/MRI images, McPET II was used to acquire the first simultaneous PET- P-31 NMR spectroscopy of an isolated perfused rat heart in the 9.4 T Bruker NMR spectrometer [23], the so-called PANDA acquisition system (PET and NMR dual acquisition). Figure 15.4 illustrates the positioning of McPET II and the NMR probe.

The use of fiber optic cables to position MRI sensitive equipment far from the magnet, and avoiding ferromagnetic material in the PET system, minimizes interference between the two imaging modalities. An analysis of the quality of MRI and PET images obtained with McPET inside the MRI revealed no significant artifacts due to such interferences [24].

2.2 Development of Solid-State Electronics

The major drawbacks of photomultiplier tubes that prevented their use in an MRI were overcome with the development of semiconductor detector technology. In particular, the development of Avalanche Photodiodes (APDs) paved the way for much of the PET technology possible today. The operation principle of an APD is based on the conversion of photon energy into free charge carriers in the semiconductor bulk, and their multiplication via the process of impact ionization. The basic element of the structure is the p-n junction. When a reverse bias is applied, a volume close to the junction is depleted of free charge carriers. The charge carriers created in the depleted region drift in the electric field towards the corresponding electrodes, and while traversing this region, acquire enough energy to produce electron–hole pairs by impact ionization. The newly created charge carriers may create new ones, and so on. Thus, there is an avalanche of electrons and holes moving through the detector. An external circuit then detects these current pulses.

Although other types of semiconductor detectors, such the pin photodiodes, were studied as an alternative to PMTs, their poor timing resolution and high noise characteristics limited their use in PET [25]. On the other hand, APDs with their reasonable timing- and energy-resolution, and, very importantly, magnetic-field insensitivity, were extremely attractive for high-resolution PET and multi-modality imaging, such as simultaneous PET/MRI. The small size and ruggedness of APDs allowed the development of PET architectures with very small crystals and high packing fraction which was not possible with traditional PMT based designs without employing light guides or the light sharing block detector techniques.

Rapid growth in semiconductor technology in the 1980s resulted in several improvements, such as higher gain and gain uniformity, due to better doping and growth techniques of the Si wafer, and higher quantum efficiency in the blue range of the spectrum (surpassing PMT quantum efficiencies) thereby making them suitable for coupling with scintillators. APDs also have an advantage over PMTs in not requiring high bias voltages to operate. Nevertheless, APDs are prone to high noise due to factors such as shot noise from internal and surface currents, capacitance noise from downstream electronics such preamplifiers, and statistical noise due to the avalanche processes. Hence, low-noise front-end electronics are required to minimize the noise and assure a good signal-to-noise ratio from such detectors. Another disadvantage is that APD gains are sensitive to temperature and, consequently, temperature monitoring or control is needed when operating APD-based devices [25, 26].

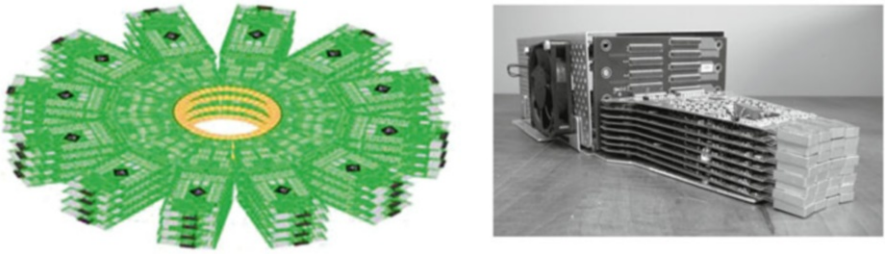

Fig. 15.5 *Left*: diagram of the Sherbrooke Small Animal Tomograph, the first LSO-APD based PET scanner (Fontaine et al. [30] used with permission, © [2005] IEEE). *Right*: a detector "cassette" making up the ring of the scanner. Reprinted with permission from Bergeron et al. [31], © [2009] IEEE

The combination of APDs with scintillators for application in PET began with Petrillo et al.'s studies of APD-scintillator detector units [26]. Using reach-through APDs (RAPDs), the first test that coupled APDs to NaI(T1) crystals, yielded an energy resolution of 10.4 % FWHM for the Cs-137 photopeak at 662 keV, with a quantum efficiency of over 50 % at NaI's emission wavelength (415 nm).

Work continued by making detector units of BGO, at that time the crystal of choice for PET scanners and APDs [25, 27, 28]. Those detector modules consisted of two individual $3 \times 5 \times 20$ mm^3 BGO crystals coupled to 4×4 mm^2 APDs. In principle, the modules could be stacked to form larger arrays. Tests demonstrated an average energy-resolution of 20 % for 662 keV Cs-137 γ rays, and a coincidence-timing resolution of 15 ns FWHM (511 keV) between two such modules, performance characteristics suitable for PET. The outcome of these and further studies was the construction of the first APD-based PET system for small animals, The Sherbrooke Avalanche Photodiode Positron Tomograph. This scanner consisted of 256 BGO APD detector modules [29] and a transaxial FOV of 118 mm and an axial FOV of 10.5 mm. Figure 15.5 illustrates the tomograph and its detector modules.

The introduction of Ce-doped LSO crystals ushered in new detector modules containing this scintillator with APDs. LSO was superior to BGO in having a much faster decay time (40 ns vs. 300 ns), hence leading to better timing-resolution. Several tests of LSO–APD detector modules established the feasibility of this approach, especially by achieving nanosecond timing resolution [32, 33]. Various detector configurations were explored, such as the one to one coupling of LSO crystal arrays to a matching APD array (Fig. 15.6) as well as position encoding using APDs [14, 34, 35]. Furthermore, progress was made in designing ultra low noise front end electronics [36, 37].

Pichler et al. evaluated the performance parameters of this LSO APD combination. Studies were conducted at 9.4 T [38] by wrapping a polished $3.7 \times 3.7 \times 12.0$ mm^3 LSO crystal in Teflon tape, coupling it to a 3 mm active diameter APD via a silicone rubber disc, and placing them in a magnet bore. The output of the APD was connected by a coaxial cable to a preamplifier also situated inside the magnet (Fig. 15.7).

Two aluminum boxes enclosed the LSO APD module, the Na-22 point source, and the preamplifier, shielding their electronics from any kind of interference from

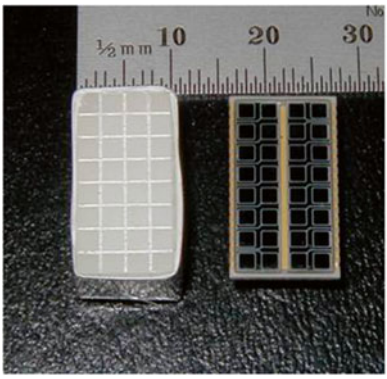

Fig. 15.6 A 4×8 LSO crystal array next to a 4×8 array of non-magnetic APDs (Hamamatsu S 8550)

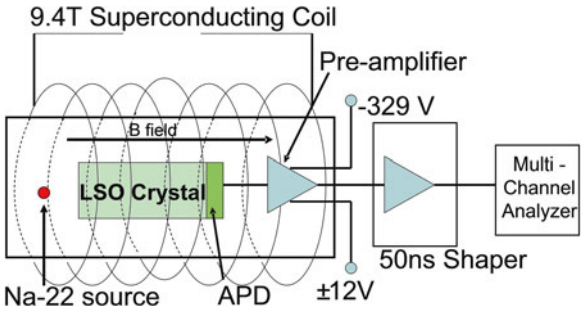

Fig. 15.7 Schematic of a LSO-APD detector module and preamplifier inside a 9.4 T magnet with the associated electronics outside the magnet

the MRI. Further, a copper tube surrounded the aluminum boxes. The output from the preamplifiers inside the magnet is fed to a preamplifier shaper outside the magnet via an 11 m long coaxial cable. Other components of the setup, such as the high-voltage supplies for the APD bias and a multichannel analyzer, were also situated outside the magnet. The study demonstrated the stable performance of the LSO APD detector module inside the 9.4 T, with no dependence in gain and energy resolution (14.4 % at 511 keV) of APD on the magnetic field. Also, there was no effect of changes in the orientation of the APD electric field with respect to the main magnetic field lines (parallel vs. perpendicular), hence proving the feasibility of operating such a PET detector module inside an MRI.

3 Current Instrumentation

Several groups developed operating PET/MRI systems for small animals, and several more formulated new technologies. In this section, we discuss current technologies and how they will take us into the future.

3.1 Current PET Systems

We have broadly classified current preclinical PET/MRI systems on the basis of the detector configuration as follows:

(a) Scintillator-PMT combination wherein the PMT is placed in a low magnetic field and light is directed into it from the scintillator via optical fibers. Section 2.1 details this system,
(b) Scintillator-APD combination that positions the APD and electronics in a low magnetic-field and directs light from the scintillator to the APD through optical fibers,
(c) Direct or closely coupled scintillator and APD detectors wherein the detector module is in the MRI's field of view (FOV), and hence experiences strong magnetic fields. Two such systems are summarized below,
(d) Silicon photomultipliers for APDs in a close coupled detector module.

In this section, we cover the design of two directly coupled APD scintillator PET/MRI systems, one developed by Judenhofer et al. at the University of Tubingen [15], and another developed by Schlyer et al. at Brookhaven National Laboratory (BNL) [39].

3.1.1 University of Tubingen Simultaneous PET/MRI Small Animal System

This PET system was built to function in a 7-T BioSpec 70/30 Ultra Shielded Refrigerated MRI, or a 7-T ClinScan MRI system (Bruker BioSpin MRI) [15]. The PET system consists of a detector module where a 12×12 array of individual $1.6 \times 1.6 \times 4.5$ mm^3 LSO crystals is coupled via 3-mm long light guides to a 3×3 APD array. The system comprises ten such detector blocks arranged in a ring. The RF coil of inner diameter 36 mm fits inside the PET ring that, in turn, fits inside the MRI gradient coil. This arrangement results in a transaxial PET/MRI FOV of 36 mm. Figure 15.8 shows the detector module and its positioning in the MRI.

The output of the APD is fed to a charge sensitive preamplifier after which it is buffered to electronics placed at a field <0.0005 T and shielded with non-magnetic coaxial cables. A copper-clad (10 μm thick) dual-sided printed circuit board (PCB) shields the detector modules. The shielded module is shown in Fig. 15.9c. These shielded modules then are assembled in a ring (Fig. 15.9b). The entire unit is positioned inside the MRI bore as illustrated in Fig. 15.9a.

3.1.2 BNL's Simultaneous PET/MRI Small Animal Imaging System

The BNL small animal PET/MRI system is based on the RatCAP technology [39]. The detector module consists of a 4×8 array of $2.2 \times 2.2 \times 5$ mm^3 LSO crystals, directly coupled to a 4×8 APD array. Each of these detector modules is mounted on a socket on a rigid flex circuit (Fig. 15.10). Twelve such detector modules on the circuit are rolled up to make the PET ring.

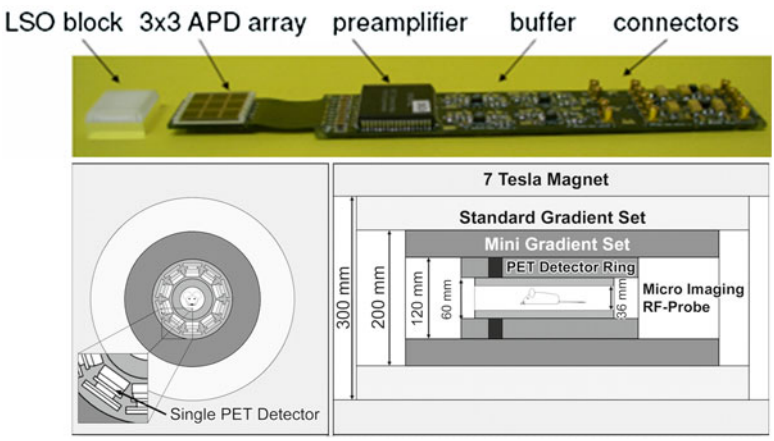

Fig. 15.8 *Top*: a detector module consisting of LSO crystals coupled to APDs and preamplifier unit printed-circuit board. *Bottom*: arrangement of PET system inside MRI showing its position between the RF and gradient coils. Adapted with permission from Judenhofer et al. [15]

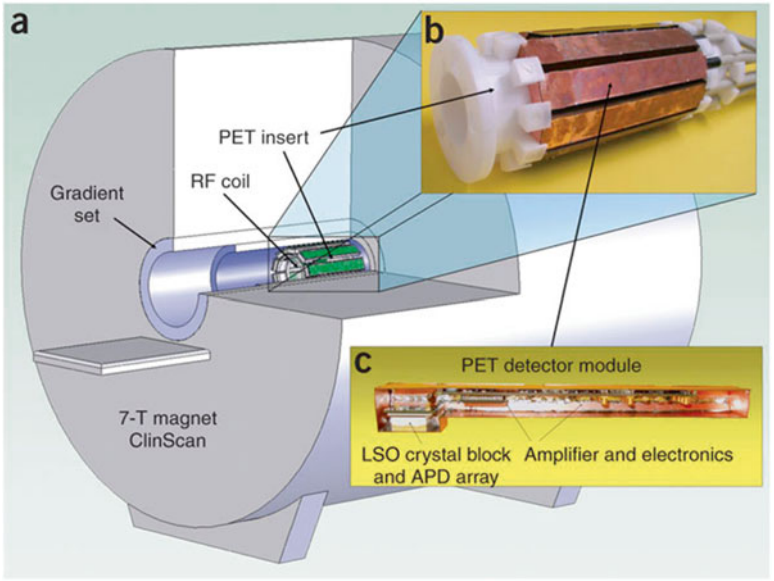

Fig. 15.9 (**a**) PET ring positioned inside scanner bore. (**b**) PET system consisting of ten shielded detector modules arranged in a ring. (**c**) PET detector module shielded by copper-clad printed circuit boards (PCBs). PET insert from the Tubingen group. Reprinted with permission from Judenhofer et al. [40])

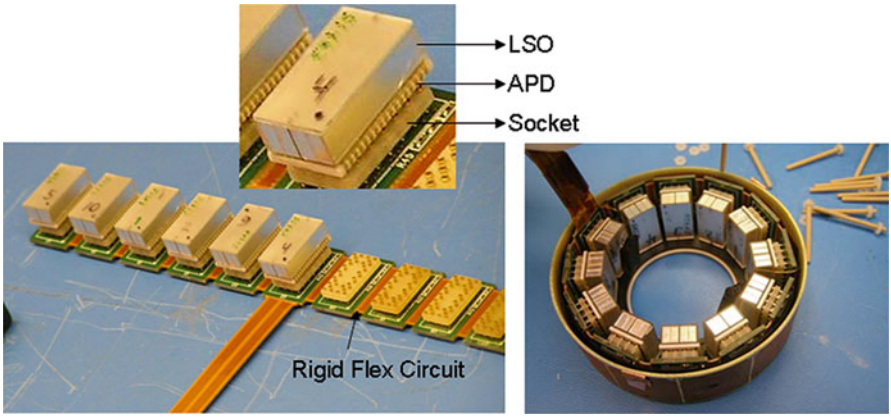

Fig. 15.10 *Left*: a rigid flex circuit partially populated with LSO-APD detector modules. *Right*: a rolled up rigid flex circuit showing the PET architecture

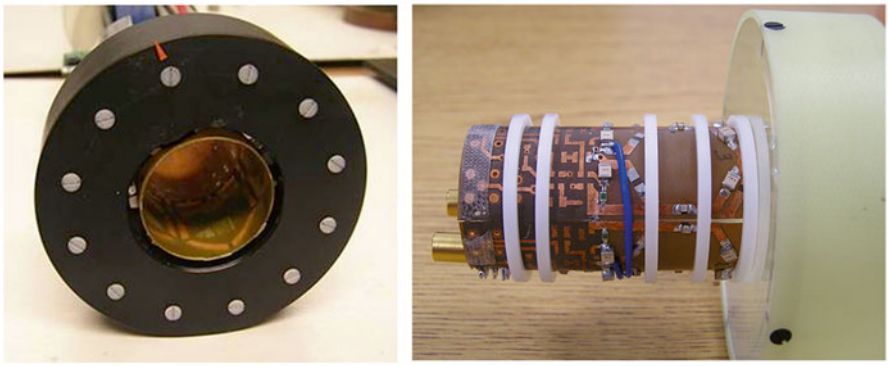

Fig. 15.11 *Left*: PET ring housed inside Delrin can with RF coil placed inside it. *Right*: the custom MRI coil used inside the PET ring

The APD signals are amplified and digitized using an application specific integrated circuit (ASIC) developed for this system [41]. The ASIC is mounted on the back of each socket on the flex circuit. The digital signal output from the ASIC is further routed to a time stamp and signal processing module (TSPM) via shielded coaxial cables; there, the events are processed further and buffered to a computer via optical fiber [42]. The TSPM is placed inside an aluminum box at the edge of the magnet bore. The power supply units and data acquisition computer also are outside the MRI room.

The PET system (Fig. 15.11) is housed in a Delrin (polyoxymethylene) plastic case, with a custom-designed RF coil that can operate in a quadrature mode positioned inside it. The PET assembly with the RF coil has a transaxial FOV of 31 mm. Cables transferring PET signals to the TSPM are housed in concentric segmented copper sheets to provide shielding and minimize eddy currents.

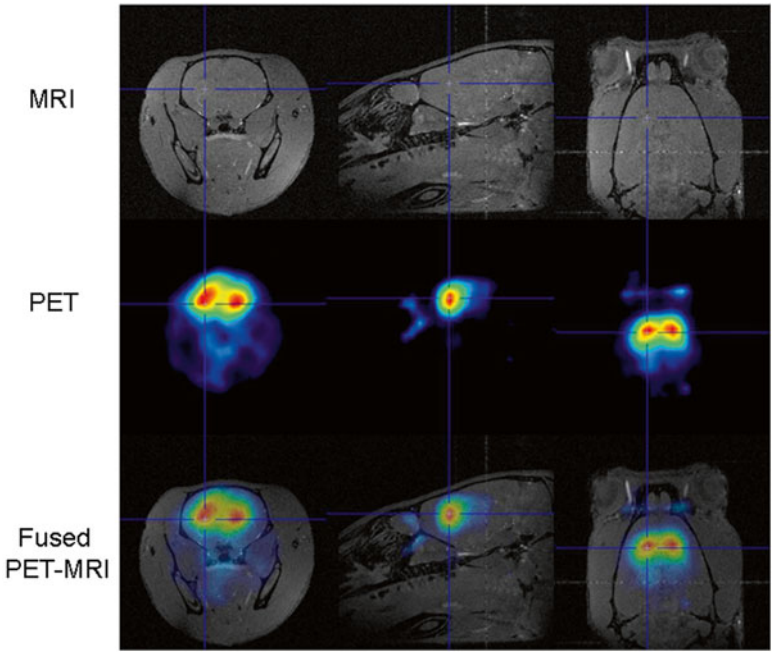

Fig. 15.12 *Top*: T1 weighted FLASH 3D isotropic MRI images of rat brain. *Middle*: PET images showing increased uptake of [^{11}C]Raclopride in the striata. *Bottom*: Fused PET/MRI images

In experiments, the PET ring and the RF coil were positioned at the center of the 9.4 T microMRI and simultaneous PET/MRI images of a rat's brain labeled with [^{11}C]raclopride were acquired. Raclopride binds specifically to dopamine receptors in the brain, and is reflected in the increased intensity of the PET signal in the brain striata, as shown in Fig. 15.12 [43].

3.2 Position Sensitive Avalanche Photodiodes (PSAPD)

One recent development in semiconductor technology for PET application was the introduction of position-sensitive APDs or PSAPDs [44]. Simply put, PSAPDs consist of a continuous layer of detector material (rather than pixelated arrays of traditional APDs) with output terminals positioned such that the relative intensity of the avalanche signal at these contacts serves to determine the exact location of the photon interaction, a principle similar to that underlying Anger logic positioning (Fig. 15.13).

With such a positioning logic, far fewer contact terminals are necessary for a PSAPD compared with a pixelated APD to achieve the same nominal spatial-resolution, thereby minimizing the electronics needed for downstream processing.

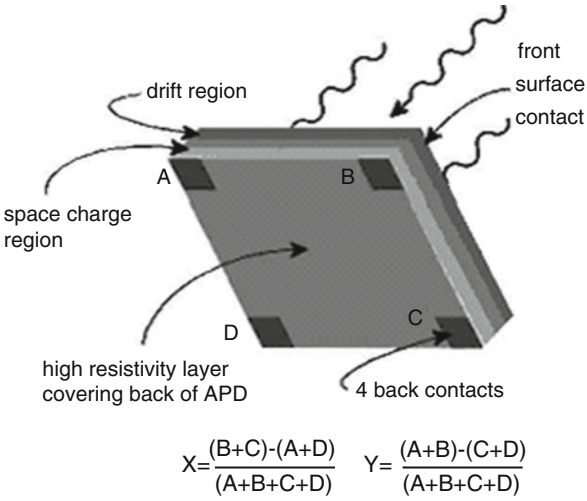

Fig. 15.13 A PSAPD with four corner-anode contacts A, B, C, D for position encoding, and a top cathode for energy and timing information. Positioning in the X and Y direction is computed for the A, B, C, D signals as shown. Reprinted with permission from Shah [45], © [2004] IEEE). For further details on the principles of PSAPDs and PET, see [45, 46]

This, in turn, reduces the cost and complexity of scanners being built using this technology, especially for small animal imaging systems where resolution is a crucial requirement, so that thousands of APD pixels have to be read out within only a small space to accommodate all the electronics. Tests with PSAPDs revealed energy and timing resolution sufficient for PET imaging and several groups have started incorporating PSAPDs into their scanner design [11, 47–49]. PSAPDs, similar to APDs, are insensitive to magnetic field and, with fewer electronics, are suitable candidates for simultaneous PET/MRI where PET detectors must fit in the space available inside a high-field MRI bore. Catana et al. implemented one such PET/MRI scanner in a 7 T magnet and acquired simultaneous PET/MRI images with it [11] (Fig. 15.14).

The PET detector in this setup consists of a module of an 8×8 array of LSO crystals ($1.43 \times 1.43 \times 6$ mm^3) coupled via optical fibers (approx. 10 cm long) to a 14×14 mm^2 PSAPDs whose terminals are further connected to charge sensitive preamplifiers (CSP) (Fig. 15.14, top). The PET ring consists of 16 modules arranged as shown in Fig. 15.14 (bottom). Concentric copper cylinders surround the CSP and associated electronics in the MRI bore minimizing electromagnetic interference between PET and MRI. The signals from the CSP are transmitted to signal processing electronics placed away from the magnet by using non-magnetic coaxial cables. The PET ring lies inside the MRI's bore between the RF and gradient coil (Fig. 15.15a). Simultaneous PET/MRI images of a mouse head acquired using this system is shown in Fig. 15.15b.

No visual artifacts were evident in the MRI images as a result of inserting the PET detectors. The effect of the MRI on PET involved a rotation in the flood histograms obtained during MRI pulsing, but unique crystal identification was still possible.

Another prominent application of PSAPDs is in depth of interaction (DOI) encoding. For small animal scanners that require high sensitivity, scintillator

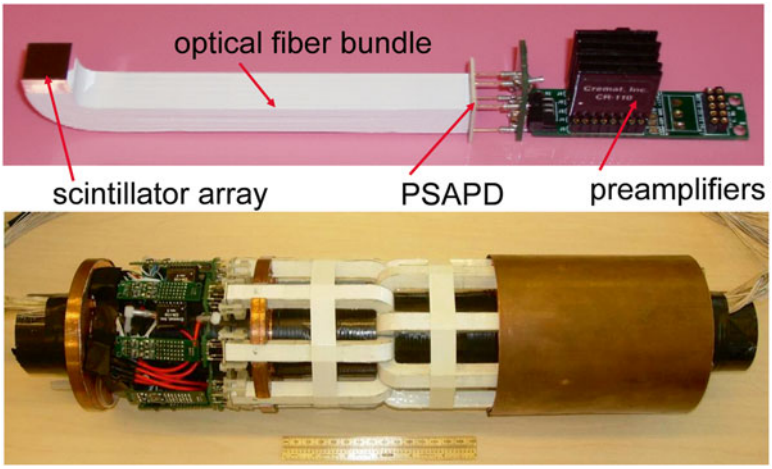

Fig. 15.14 *Top*: a detector module consisting of an LSO array coupled to PSAPD using optical fibers. *Bottom*: PET detector ring consisting of 16 such detector modules shielded with copper. (Photographs courtesy of Simon Cherry)

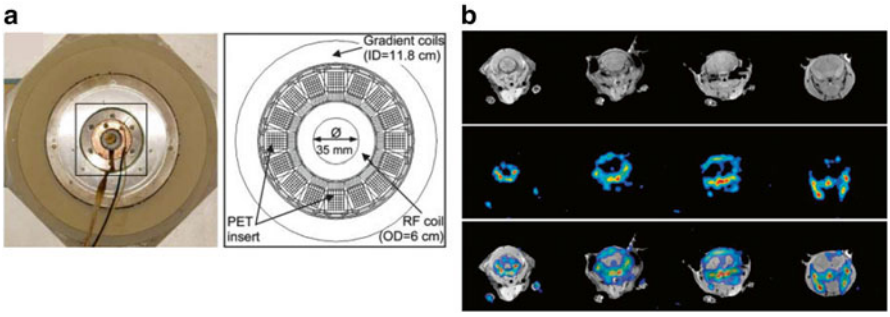

Fig. 15.15 (**a**) Arrangement of PET detector inside MRI's bore. (**b**) Simultaneous PET/MRI images of a mouse head using ^{18}F showing uptake of the radiotracer in the bones. *Top row*: MRI images, *Middle row*: PET Images, and, *Bottom row*: Fused PET/MRI images. Reprinted with permission from Catana et al. [11]

crystals need to be long (10–20 mm) to stop more annihilation gammas, and the detectors must be placed very close to the imaged object to increase solid-angle coverage. However, the combination of these two factors can result in severe parallax errors. With fewer electrical contacts and low gamma attenuation properties, depth of interaction encoding is feasible by placing PSAPDs on two opposite faces of the scintillator crystal. Several studies demonstrated the DOI encoding capabilities of PSAPDs [50, 51] thereby improving the spatial resolution attainable. Hence, PSAPD detectors can support high-sensitivity, high-resolution MRI compatible PET scanners.

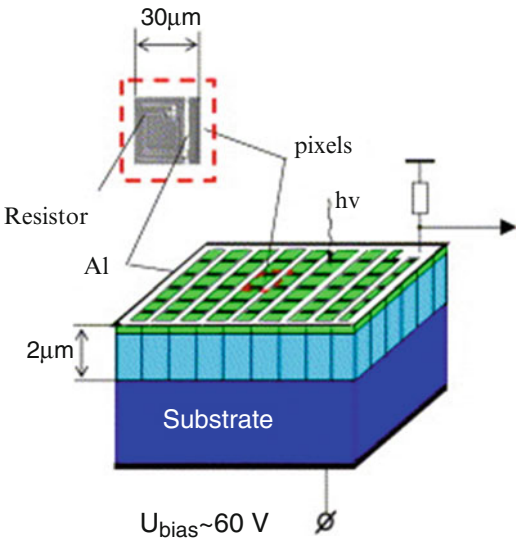

Fig. 15.16 A SiPM array consisting of several micropixels on a common substrate. Adapted from [53]

3.3 Silicon Photomultiplier

The Silicon Photomultiplier (SiPM) is a promising new technology that combines the high-gain, low-noise properties of a photomultiplier tube with the magnetic insensitivity of an APD. Also known as the Geiger Mode APD, these devices are, as the name suggests, APDs operating at a bias voltage slightly above their breakdown point, or in the Geiger mode [52]. Consequently, SiPMs exhibit very high internal gains on the order of 10^5–10^6, and have timing properties that act as a single-photon counter. Figure 15.16 illustrates the typical structure of a SiPM array. The array comprises a few hundred to a few thousand microcell or micropixel APDs on a common substrate of 1×1 mm^2.

An incident photon triggers the production of a charge carrier that, in turn, creates an avalanche breakdown. The SiPM is essentially a photon counter, and generates a standard output signal for one or more photon interactions per cell. This is where the structure of the microcell array, and the detector's single-photon counting capability come into play. With multiple photon interactions over a given area, multiple microcells are triggered into avalanche breakdown. Hence, the number of microcells fired in the array is proportional to the number of photon interactions taking place. This is true only if the rate of incoming photons is such that only a single photon interaction occurs in a microcell within its quenching time, i.e., the period it takes for a microcell APD to come back to its normal state after an avalanche breakdown. Passive quenching is achieved by connecting each of the microcell APDs in the series with a resistor to a common aluminum grid for reading out the signals from the array. The resistive layer also acts as a decoupling element between the adjacent microcells in an array. However, it also reduces the active area of the SiPM array, thereby reducing its overall detection efficiency.

From the perspective of using these detectors for PET, the following are its key advantages:

1. High intrinsic gain and low excess noise,
2. Insensitivity to magnetic field (particularly suitable for PET/MRI imaging),
3. Good timing-resolution (in picosecond range),
4. Low temperature-dependence compared traditional APDs,
5. Low operating voltages,
6. Low production costs.

Studies of SiPMs with scintillator crystals, such LSO/LYSO for PET have demonstrated good energy and timing resolution along with the listed favorable properties [53–55]. However, one drawback of SiPMs is their low detection-efficiency at the LSO/LYSO emission wavelengths (or the blue end of the spectrum). Hence, more work is needed here to fully exploit their usefulness for PET.

3.4 Modified MRI Scanner Architectures

Until recently, most work combining PET and MRI focused on modifying PET instrumentation to fit and function inside an existing MRI scanner. However, PET/MRI scanners have been designed wherein the MRI scanner instrumentation was modified to accommodate PET detectors. We describe two such systems below.

3.4.1 The microPET®-MRI System

The microPET®-MRI system, as the name suggests, implements the architecture of the microPET® (Focus 120) small animal scanner inside an MRI [5]. The MRI scanner is a novel 1 T superconducting magnet, fabricated in two halves with an intervening 80 mm gap, i.e., in a "split magnet" design that accommodates the PET detector modules in the gap. The modules, consisting of LSO crystals (12×12 array) are coupled to a position-sensitive PMT through optical fibers in a ring architecture. Figure 15.17 is a schematic of this arrangement.

As the illustration shows, the PMT is positioned outside the magnet bore at a radial position of 120 cm (length of optical fibres) where the field strength is about 30 mT. The PMTs are further shielded with soft iron, reducing the field strength experienced at the PMT to 1 mT. This configuration, with PET detectors positioned in the center of the MRI, supports simultaneous PET/MRI. There was minimal degradation in the sensitivity and energy spectra obtained from the PMT due to the magnetic field. However, using 120 cm long fiber-optic cables causes some degradation in energy resolution from loss of light. MRI images of a mouse brain obtained using this split magnet scanner verified that it generates good-quality, high-resolution images.

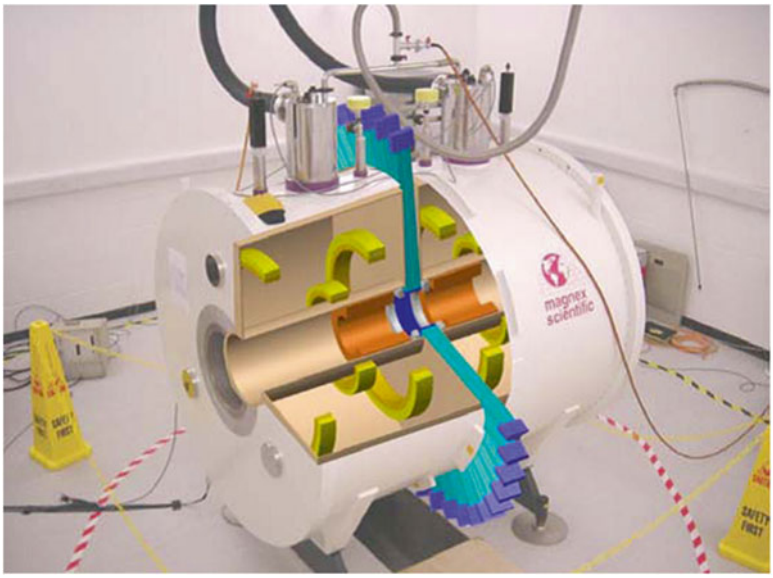

Fig. 15.17 Schematic drawing of PET detectors positioned in the split magnet space of the MRI. Reprinted with permission from Lucas et al. [57], © [2006] IEEE

3.4.2 Field Cycled MRI-PET System

The principle of operation of a field-cycled MRI-PET system is that PET data is acquired when the MRI magnetic field is turned off or cycled to zero [58]. This practice avoids the limitations faced when attempting to operate traditional PET systems in a magnetic field. A field-cycled MRI consists of two sets of magnets. The first one, called the polarizing magnet, is a high-strength magnet that polarizes the objects placed in its field of view. After polarization, this magnet is cycled to zero and the second magnet, a low field strength readout magnet is activated such that the polarized volume is precessing at the Larmor frequency of the readout magnet. During the readout magnet phase, excitation and readout pulse sequences are carried out by pulsing the RF and gradient coils. This phase of the pulse sequence is followed by a period when the readout magnet is cycled to zero and the magnets are allowed to cool, during which period, the PET images are acquired. Since there is no magnetic field during this period, readout can be accomplished by placing the PMTs in the field of view, hence allowing direct coupling and avoiding the use of light guides that degrade the PMT's performance. Gilbert [59] proposed this design (Fig. 15.18). A gap of 9 cm in the MRI system accommodates the PET system.

Other advantages of this mode are reduced distortion due to the magnetic field's homogeneity because the readout magnets are of low field-strength. This feature also reduces the requirements on RF and gradient power, thereby lowering their impact on the PET's electronics in comparison with standard high-field MRI systems.

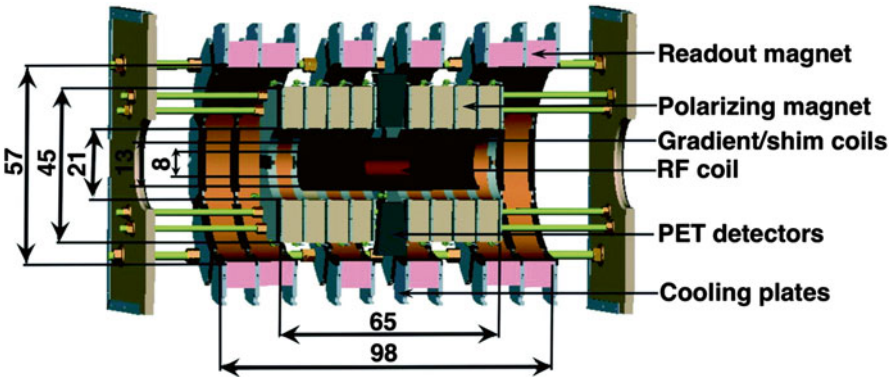

Fig. 15.18 Schematic of a field-cycled MRI with PET detectors. Reprinted with permission from Gilbert et al. [59]

4 MRI and PET Data Acquisition System Interactions

Potential interactions between the MRI system and the PET system could degrade their respective images. Interferences and artifacts might appear in the MRI images from the PET's electronics, and excess random counts in the PET's data stream might be created by the magnetic and radio frequency characteristics of the MRI data acquisition system. In this section, we a look at some potential interferences and describe different approaches to minimizing or eliminating them.

4.1 Shielding Approaches

There are three basic approaches to minimizing interference between the PET's electronics and the MRI data-acquisition system. The first is to move the electronics away from the MRI data system. This approach uses optical fibers to transmit the light from the scintillation crystals to the light detection devices, either PMTs or APDs. The second approach uses heavily shielded PET electronics situated inside the bore of the magnet and in close proximity to the MRI transmit and receive coils. This is the approach that has been used in the commercial PET system developed for human use and has also been employed for small animal scanning [12]. The third approach uses minimal or no shielding between the PET and MRI. This allows the maximum sensitivity for the MRI, but can result in a significant number of random counts in the PET system caused by the effects of the gradient fields and the RF pulses on the PET electronics.

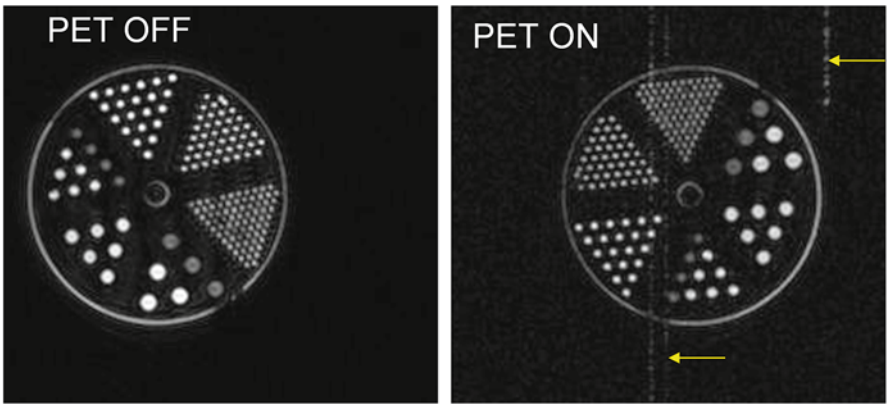

Fig. 15.19 MRI images and profiles of a resolution phantom containing water in some compartments and fat in others, without a PET system (*left*) and with a PET insert in place and powered on (*right*). Notice the line artifacts marked with the *yellow arrows* in the MRI image in the upper right and extending through the center of the image

4.2 Degradation of the MRI Image Due to PET Inserts

Using the configuration with light fibers and remote electronics seemingly guarantees minimal interference in the MRI images. In a study using a prototype MRI compatible PET system, subtraction images were used to delineate artifacts in the MRI images and none were observed [60]. Placing PET detectors and electronics that might contain metal components inside the MRI magnetic field can compromise the magnetic field's homogeneity, and may result in artifacts in the MRI images. Photodiodes or avalanche photodiodes are compatible with magnetic fields, but the acquisition of artifact free MRI images with these devices require assuring that components that do not contain any ferromagnetic materials.

In some PET systems, the PET events are timed using a high frequency "clock" signal that is propagated through the electronics on the PET insert. In this configuration, the clock signal might interfere with the MRI signal if the frequencies are close to each other, or are harmonics of each other. Offsetting the frequencies some amount will reduce the interference greatly. We studied the effects of PET electronics and hardware on MRI images with a 1.5 T MRI. These tests were performed without power on the PET circuits to demonstrate their potential effect. We filled one row in a Mini Deluxe Phantom (Data Spectrum Corporation, NC USA) hot spot insert with vegetable shortening to mimic fat, and the rest with 1 mM $CuSO_4$ solution. Figure 15.19 shows MRI images of the center slice of the phantom with no PET insert and with PET inserted and turned on. Yellow arrows mark the artifacts.

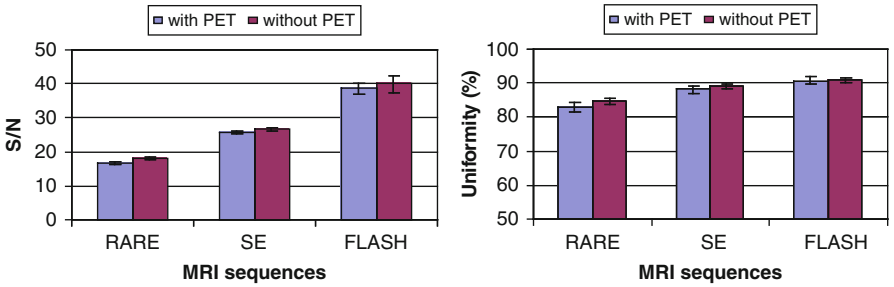

Fig. 15.20 Comparison of MRI image characteristics with and without the PET inserted (Plot courtesy of Simon Cherry)

Accordingly, we demonstrated that good MRI images are obtainable without RF shielding. Mild artifacts due to interference are represented in the form of streaks on the image. With RF filtering, we were able to eliminate these artifacts

Using shielding on the PET insert will allow essentially noise-free MRI images. Figure 15.20 plots the results of a study by Simon Cherry (private communication) on the signal-to-noise ratio in the MRI images; it shows the uniformity of this ratio as a function of the pulse sequence.

4.3 MRI Effects on Spatial and Temporal Resolution of the PET Images

Using the configuration of shielded light fibers and remote electronics, apparently there is minimal interference in the PET images. When the electronics are placed inside the MRI scanner, there can be significant effects. Using an unshielded case for the RatCAP and taking data in the 9.4 T magnet, we observed the following interference [39]. A very clear noise signal was generated in the unshielded PET electronics from the RF pulse sequence as shown in Fig. 15.21. The figure illustrates MRI pulse sequence on the upper part of the figure and the PET single counts below.

There are two ways to overcome this problem. The first is to remove the noise from the data by gating out the RF pulses, out. The second is to carefully shield the PET electronics from the RF pulse sequence. Figure 15.22 illustrates a case that we designed at BNL for this purpose.

The shield is constructed of G-10 material with a thin (5 μm) copper layer on the surface to block penetration of the RF power. The shielding is segmented to reduce eddy currents, and the electronics are placed inside a secondary shield shown on the right hand side of the figure.

In PET/MRI scanners that use shielded, short optical fibers and APDs, the number of counts per second is constant as the gradient coils are operated. Figure 15.23 plots the number of PET counts recorded as the gradient coils are turned.

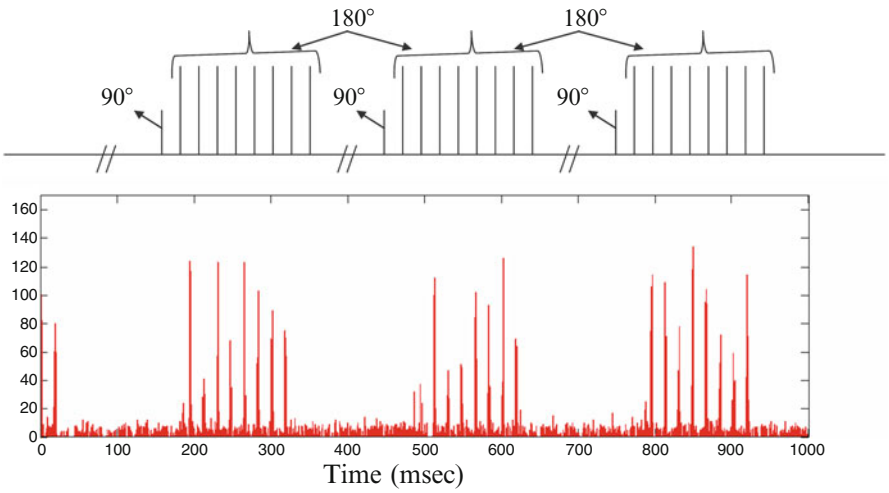

Fig. 15.21 PET data showing the noise introduced by the RF pulse sequence in an unshielded PET scanner

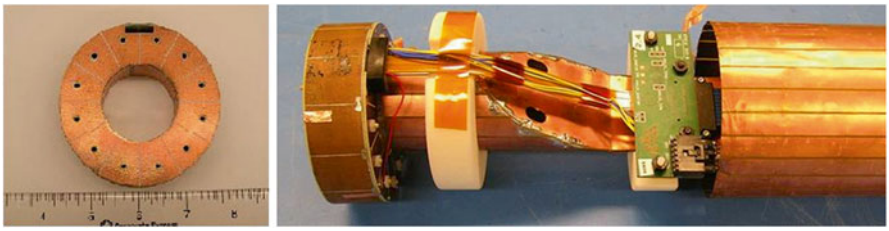

Fig. 15.22 *Left*: RF-shielded case for the RatCAP scanner used in the 9.4 T magnet at BNL; *Right*; RatCAP with RF shield before sliding the outer shield over the entire assembly

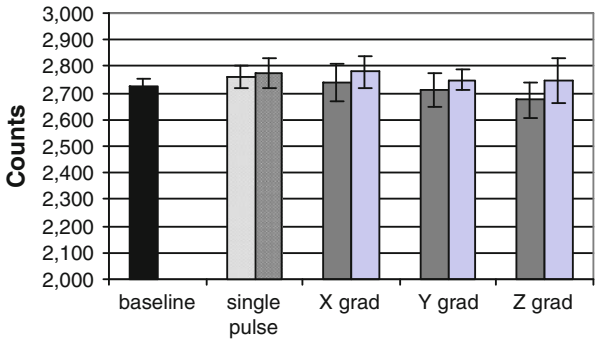

Fig. 15.23 Plot of number of counts during operation of the MRI gradient coils. *Dark gray bars* indicate that the gradients are off, and the *lighter blue bars* show that the gradients are on. (Plot courtesy of Simon Cherry)

4.4 PSAPD Detector Efficiencies in Magnetic Fields

Position Sensitive Avalanche Photodiodes (PSAPDs) provide similar noise, gain and quantum efficiencies to single channel APDs, but employ charge sharing amongst anodes to obtain position information. Only five contacts are needed to identify the position of the photon interaction, thereby greatly simplifying the electronic circuitry. In summary, PSAPDs offer good resolution in energy, timing, and space, and have greatly reduced electronic readout requirements.

When a uniform flood source is imaged in PET tomographs that use PSAPDs, the positional information is typically somewhat distorted showing a "pincushion" effect. This effect is a result of the Anger logic used to decode the position of the event using the four electrodes on the resistive sheet that comprises the PSAPD. This can complicate accurate segmentation of crystal positions if the distortion is very severe. Methods have been developed to correct for this effect [61].

The major potential problem of placing the PSAPD in the magnetic field is that the "pincushion" distortion may become more severe and events will be mispositioned and the energy resolution compromised due to the distortion from the magnetic field. In calibrating a PET system, the individual crystals are mapped by using a look-up table to normalize for the individual crystal's characteristics, such as energy, coincidence time-windows, and efficiencies. Plotting the maps in the magnetic field and applying this correction consistently eliminates such mispositioning. The only added complication is distortion due to the gradient fields. These effects were explored and algorithms developed to minimize the effects and produce an accurate segmentation of the crystals, even down to 1 mm resolution [61–64].

4.5 Magnetic Field Effect on Positron Range

Researchers have studied the effects of the magnetic field on the range of the positrons. Since the positrons' range is one of the limiting factors in the ultimate spatial resolution obtainable with PET, any improvement in it is an added benefit of the MRI environment, although this applies only in the 2-dimensional plane perpendicular to the magnetic field.

Raylman's Monte Carlo study [65], demonstrated that a substantial improvement in resolution can be achieved for higher energy positrons. Table 15.1 lists the findings for F-18, C-11, O-15, and Rb-82.

Raylman noted that there was some degradation in the annihilation non-collinearity that will degrade the resolution in large PET scanners, but which will be less important with a smaller diameter ring. There have been some experimental measurements of the improvement in spatial resolution in PET with magnetic fields [4, 66]. Using germanium-68 as the source of high energy positrons (Emax = 1.89 MeV), the results in Table 15.2 were obtained. These values are the ratio of the full width at half maximum of the point-spread function (PSF) in the

Table 15.1 Maximum positron energy and resolution change with and without an applied 10 T magnetic field [65]

Radionuclide	Max energy (Mev)	FWHM (0 T) (mm)	FWHM (10 T) (mm)
F-18	0.64	3.85	3.78
C-11	0.96	4.24	3.85
O-15	1.7	5.28	3.88
Rb-82	3.15	8.03	4.13

Table 15.2 Ratio of the full width at half maximum (FWHM) of the point spread function (PSF) with the field off, divided by the FWHM of the PSF with the field on as a function of magnetic field for Ge-68 in water

Field	$\frac{\text{FWHM off}}{\text{FWHM on}}$
0 T	1.0
4.0 T	1.22
5.0 T	1.42
9.4 T	2.05

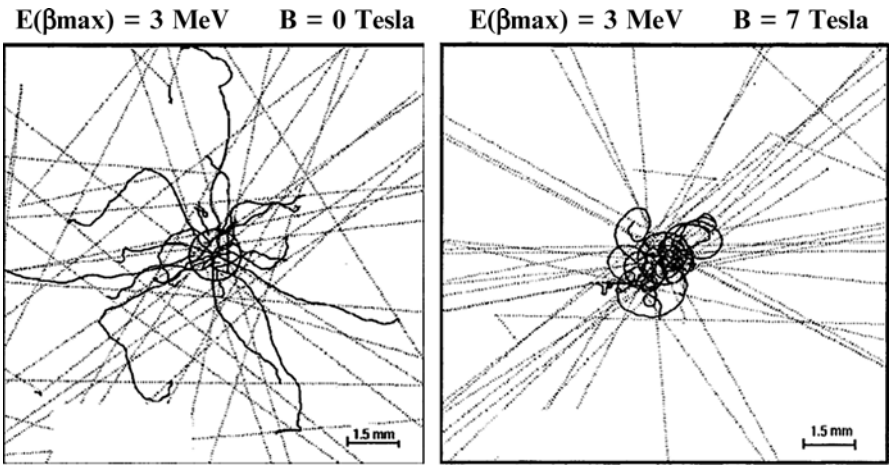

Fig. 15.24 Range of positrons with no magnetic field (*left*), and in a 7 T magnetic field (*right*). Reprinted with permission from Wirrwar et al. [68], © [1997] IEEE

transverse direction with the magnetic field off, divided the same measure with the magnetic field on as a function of the magnetic field (Table 15.2) [67].

A similar study, one with a very high-energy positron (3 MeV) and a 7 T magnet [68] encompassed theoretical and experimental measurements. Figure 15.24 is a graphical representation of the data generated from the GEANT simulation.

4.6 MRI Images for PET Attenuation Correction

One key advantage of PET is the possibility of gathering quantitative information on the distribution of radioactivity inside an object. However, for PET data to be quantitative, it is necessary to correct for the attenuation of the gamma rays as they pass through the object being scanned. The key characteristics of a material determining gamma attenuation are its atomic number and the electron density. When PET was being used alone, the attenuation was measured directly with either a ring source or with one or more rotating sources containing a positron emitter (usually Ge-68). Since the advent of PET/CT, the correction for attenuation is based on the data from the CT scan. This generates a relatively accurate attenuation map, although some concerns remain, such as the difference in attenuation of the 511 keV gammas compared to the attenuation of the much lower energy X-rays used in CT imaging.

With the move to MRI as the PET's complementary imaging modality, the attenuation correction must be based on the data available. A problem arises because the MRI signal is related to the proton density and not directly related to the electronic density that determines gamma attenuation in an object. Several approaches have been developed to obtain the attenuation map from MRI data and these methods are discussed here.

The attenuation of gamma rays by matter is a function of the electron density of the material through which they pass. Attenuation differs, depending on the energy of the gammas and the different processes contributing to attenuation. The X-ray CT maps are obtained with X-rays with maximum energy of 140 keV, while attenuation must be corrected in PET for photons of 511 keV. Thus, the attenuation-correction algorithm must convert the attenuation coefficients for 140 keV derived from CT maps, to the coefficients of 511 keV. This conversion may affect the accuracy of the attenuation corrected PET image for different tissue densities normally encountered in clinical studies such as lung and bone. However, in clinical practice the CT attenuation map often is more accurate than the traditional Ge-68-derived one, even with the extrapolations made due to the differences in energy, because the noise level of the CT image is very low, and therefore yields a very accurate map of the object.

The usual method in MRI is to segment the image in some way and then assign values for the attenuation based on this segmentation [69, 70]. One approach is to use the MRI image directly and assign different average values of attenuation for regions of bone, soft tissue, and air. There may be more regions, depending on the required level of complexity. An alternative is to obtain a CT attenuation map for several patients, and form an averaged attenuation map with the corresponding attenuation values. This attenuation map is then transformed (stretched and adjusted) to match the MRI image of the particular patient. This attenuation correction is then applied to the PET image to get an attenuation corrected image. This population based approach has some advantages and some disadvantages. The advantages are that it is relatively easy to implement, and does not require any additional scans. The disadvantages are that the general template must be adjusted for each patient using some either manual or automated fitting and that there is no easy way to adjust for differences in bone density.

Table 15.3 Typical attenuation coefficient values for MRI segmented

Region	Typical values (cm^{-1})
Brain	0.095–0.099
Skull	0.143–0.151
Nasal sinuses	0.054–0.055
Soft tissue, and skin	0.095–0.096

The most common approach for MRI attenuation correction of PET images is using some type of segmentation. The parameters employed for segmentation and the number of components determines the model's sophistication and accuracy. The simplest method of attenuation correction without using a transmission scan is to apply a uniform attenuation coefficient throughout the volume being imaged. For the brain, a simple elliptical model is often used. There was an improvement in the accuracy of the PET data using this approach, but it did not produce quantitative values. Early attempts to use MRI data to give an attenuation map followed that methodology [71]. The method was enhanced by adding more types of tissue with better estimates of the attenuation coefficients [72]. Table 15.3 gives typical segmentation values for these parameters for imaging several organs and tissues.

Correcting PET data for attenuation using MRI images still is being investigated actively. Several reviews [72–74] examined the possibilities and covered the work already done. The general conclusion is that using MRI for attenuation correction certainly is not as straightforward as using CT, but should be possible. Segmenting the skull into several regions and assigning attenuation coefficients seems to work well. For the torso, the favored approach seemingly is to fit the MRI images to a standard atlas by adjusting the standard organ sizes and shapes to match the patient.

5 Prospects for the Future

The first steps have been taken in the development of simultaneous PET/MRI scanners. There is a great deal left to do in terms of instrument improvements and the applications are just beginning. This is a very exciting time in multi-modality imaging that promises to get better.

5.1 Technical Challenges Still Ahead

Several technical challenges must be overcome before simultaneous PET/MRI is a mature technology. The ultimate goal is to design a system where the MRI does not degrade the PET image significantly, and the PET electronics do not interfere with the MRI electronics causing artifacts or decreasing the signal-to-noise in the MRI images. The greater the distance between the two systems, the easier this goal is to realize. Even a few millimeters will greatly reduce the interaction between the two

systems. Any conductive materials in the PET part of the system will need to be compensated by tuning the RF coil with the PET insert and object in place. For this reason, it is important to be able to tune the coil remotely from outside the machine.

Another consideration is the sensitivity of the gain of APDs to changes in temperature. Typically, a few degrees shift in temperature alters the gain by a large factor. The switching gradient's magnetic field and RF pulse sequences sometimes cause a notable rise in temperature from interactions with the PET system itself due to eddy currents, or even with the object being scanned. A temperature compensation mechanism should be incorporated in the PET electronics to deal with temperature drifts. PET electronics generate noise that can be picked up by the sensitive receivers in the MRI system. This is particularly true if there is a clock frequency running in the PET electronics to supply a timing signal. The frequency of this clock must be different from the MRI's fundamental or harmonic frequencies because the receivers are tuned specifically for this frequency and therefore, are particularly sensitive in this range. In our experience, the difference between 100 MHz and 105 MHz can be crucial for a 400 MHz (9.4 T) MRI system in terms of the signal-to-noise ratio of the MRI images.

5.2 MRI Spectroscopy with PET

Figure 15.25 shows a specific potential application of our hybrid PET/MRI system in a small-animal model. This mouse study illustrates how MRI spectroscopy, which can image flux rates throughout the tricarboxylic acid (TCA) cycle, when combined with PET, will afford a temporal correlation that is critical in meaningfully comparing these two functional datasets.

5.3 MRI Dynamic Domain Compared to PET Dynamic Domain

One interesting aspect of combining PET with MRI is the comparison of their time domains. The quality of a PET image mainly rests on the number of counts in it. It makes little difference if those counts are acquired over a few seconds or over several hours (neglecting deadtime considerations). MRI, on the other hand, has relatively constant signal and the accessible time-domain depends on the strength of the magnet, the pulse sequence used and, the relaxation constants of the environment.

One advantage of MRI is that an indefinite number of repeat studies can be done, so longitudinal studies are easy. On the other hand, for such studies in PET, with its short-lived positron emitters, usually necessitates two, three, or more injections of the radiotracer.

Under the right conditions the temporal information gained from PET can be closely correlated with the information from MRI. As an example of this, the study of brain function in small animal models requires both the localization of neural activity and the time sequence of the activation. Neuronal activation consumes

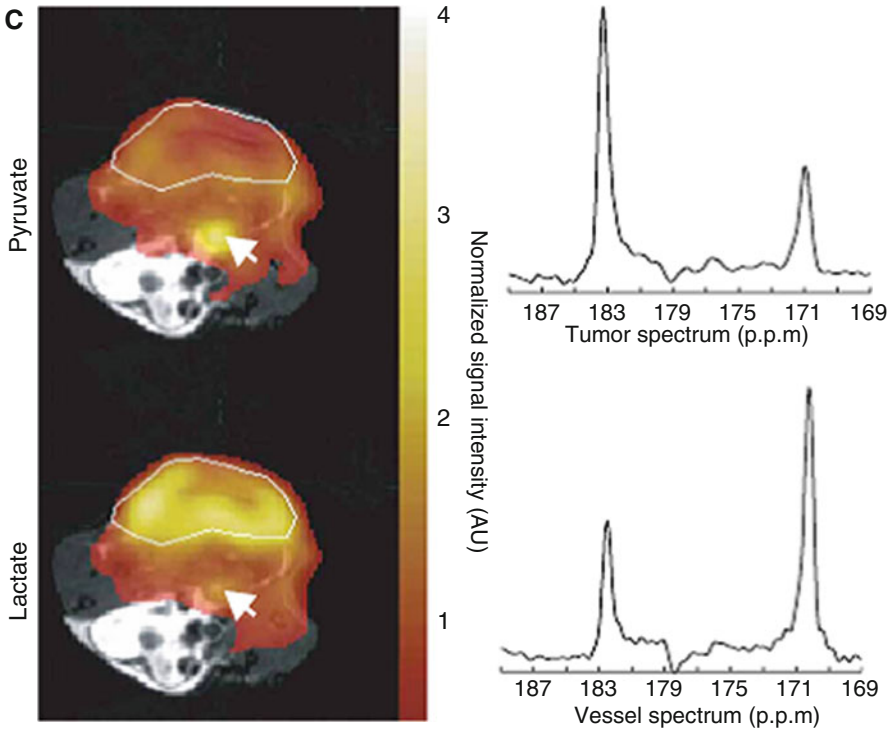

Fig. 15.25 Hyper-polarized ^{13}C-MRS in mouse-tumor imaging. Color maps representing [1-^{13}C]-lactate and [1-^{13}C]-pyruvate peak intensities and spectra from the tumor and a blood vessel (indicated by *arrow*) in mouse treated with an etoposide (chemotherapeutic agent). The ^{1}H images, shown in grayscale, were used to define the tumor's margins (indicated by *white lines*). Reprinted with permission from Day et al. [75]

oxygen [76]. After neural activation (particularly in the cerebral cortex), an increase in blood flow produces an influx of oxygenated hemoglobin. This influx reduces the local concentration of deoxygenated hemoglobin (deoxyhemoglobin). This effect is called the hemodynamic response (HR). This reduction can be measured using BOLD fMRI (blood oxygen level-dependent functional magnetic resonance imaging) [77], which now is the most popular method in functional magnetic resonance imaging (fMRI) and serves as one of the major experimental methods for analyzing neural function. However, vascular processes take at least an order of magnitude longer time than the underlying functional activation. The time-to-maximum of a HR due to a transient stimulus is typically delayed by 5–8 s and dispersed by 3–4 s. Oxygen-15 and PET can be used to correlate with the BOLD signal. This is a relatively new area, but promises to give new insight into neural activation. Oxygen-15 studies have been used extensively for the analysis of stroke in humans [78] although the possibility of doing both PET and MRI simultaneously will add a new dimension to these studies.

5.4 Preclinical and Research Applications

Imaging protocols are currently under development where MRI and PET are used in conjunction either to monitor the same physiological parameter for cross-validation, or to monitor different stages of metabolic activity and thus, different targets. We give examples of these types of investigations below.

A goal of neurophysiology is connect behavioral results with observables of non-specified or background mental functions, like awareness. The successes of PET and fMRI in non-invasively localizing sensory functions encouraged researchers to transform the subjective concepts of cognitive psychology into objective physical measures. Experimental results are interpreted in terms of flexible definitions of both cognitive concepts and the degree of localization. New approaches may connect measurements by fMRI, ^{13}C MRS, and PET of brain energy with observable behavior or more elusive parameters such as awareness. A sensory stimulation experiment could show whether the degree of localization found in BOLD signals is related to the global energy of the brain, which, when manipulated by anesthetics, will affect the degree of awareness. The influence of brain energy upon functional imaging maps is changing the interpretations of neuroimaging experiments [79]. Gerstl et al.'s study [80] is another example of correlating the regional distribution patterns of transmitters and the observable functional fields of the brain using fMRI and PET. They found that the distribution pattern of the major inhibitory serotonergic neurotransmitter-receptor, the 5-HT1A subtype, measured by PET is associated with the functional organization of the primary and secondary visual cortex defined by retinotopic mapping with fMRI. This work demonstrated study showed that multimodal neuroimaging combining PET and fMRI can clarify the relationship between the distribution of neurotransmitter receptors and functional specialization in human cortical areas in vivo.

One exciting area for combining PET and MRI is the ability to carry out functional and morphological imaging simultaneously. A specific example is employing advanced MRI techniques, such as diffusion tensor imaging (DTI), to delineate nerve tracks and correlate this with PET activation of nerve cells. This approach was used to demonstrate the invasion of tumor cells into pyramidal tracts and relate this information to the uptake of the PET tracer ^{18}F-fluoroethyl-L-tyrosine that measures cell proliferation [81]. Such data could prevent the destruction of important structures through more precise preoperative planning.

As another similar example of the complementary nature of PET and MRI is in ischemic stroke, where diffusion-weighted (DW), and perfusion-weighted (PW) magnet resonance imaging (MRI) are used to define the therapeutic target as the mismatch between the two volumes. Positron emission tomography (PET) can quantify the metabolic patterns of tissue compartments identified using this MRI technique. In one such study, the mismatch area did not reliably detect elevated Oxygen Extraction Fraction and overestimated the penumbra defined by PET [82].

Oxygen-15 labeled water imaging has become the gold standard for assessing cerebral blood flow (CBF). A new technique, arterial spin labeling (ASL), makes

it possible to measure CBF accurately with MRI without using contrast agents. In ASL, arterial blood water is first magnetically labeled just below the region (slice) of interest by applying a 180° radiofrequency (RF) inversion pulse which inverts the net magnetization of the blood water. After a period of time (called the transit time), this 'paramagnetic tracer' flows into the slice of interest where it exchanges with tissue water. The inverted spins carried with the blood coming into the volume of interest reduce total tissue magnetization. During this time, an image is taken (called the tag image) which highlights the change. The primary advantages are that completely noninvasive, absolute cerebral blood flow (CBF) measurements are possible with relative insensitivity to permeability, and that multiple repeated measurements can be obtained to evaluate one or more interventions or to perform perfusion-based functional MRI [83]. In one study, three patients with epilepsy and tuberous sclerosis underwent brain MRI with ASL and positron emission tomography (PET). The results were closely correlated with each other and with electrophysiological data [84]. Chen et al. [85] compared cerebral blood flow changes (ΔCBF) measured with flow-sensitive alternating inversion recovery (FAIR) ASL perfusion method to those obtained using $H_2{}^{15}O$ PET, the current gold standard for in vivo imaging of CBF. They imaged a group of healthy volunteers under identical conditions to study changes in regional and global CBF during five levels of visual stimulation and one level of hypercapnia. The CBF changes were compared using three types of region-of-interest (ROI) masks and found to be closely correlated [85].

There is some correlation between the size of the hippocampus and the development of Alzheimer's disease. Recently, a PET compound was developed and patented by researchers at the University of Pittsburg (Pittsburg Compound B or PIB) that apparently is a marker for amyloid plaque. One study aimed at relating the size of the hippocampus, the uptake of PIB, and the degree of cognitive impairment in an older population [86]. This study gives a preview of how anatomical detail as measured by MRI can be correlated with activation, enzyme concentration, or other measures physiological processes to give a clearer correlation between structure and function.

In a further application of simultaneous PET/MRI images, obtained with the Tubingen system, of the uptake by a mouse colon carcinoma [40] revealed selective uptake in its viable regions compared with degenerate areas (Fig. 15.26).

The corresponding MRI images also show increased contrast uptake in the viable regions of the tumor, while, at the same time, providing high-resolution structural information. Hence, the combination of PET/MRI accurately localizes the viable region versus regions with inflammation or necrosis on the tumor.

5.5 Multimodality Probes

Based on the discussion, it is clear that the total information that is obtained using PET and MRI simultaneously is greater than the sum of the parts. For PET and MRI probes to be truly simultaneous, they must have identical pharmacodynamic

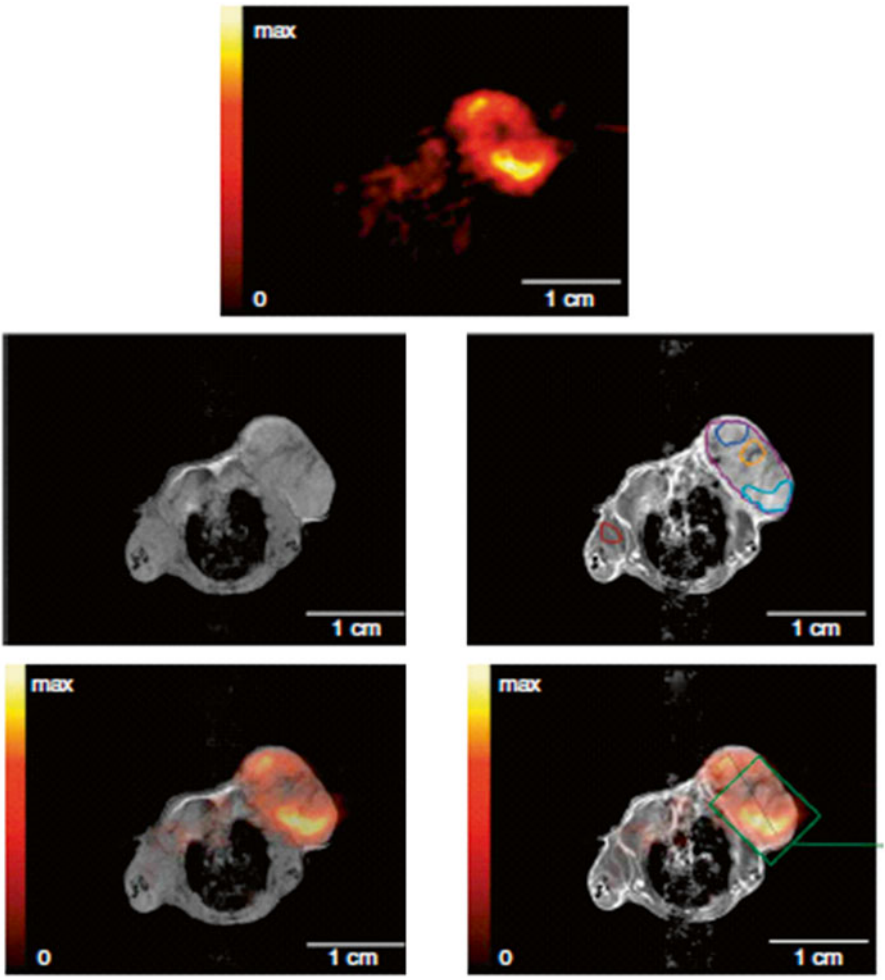

Fig. 15.26 *Top row*: F18- FLT PET image of colon carcinoma uptake. *Middle row*: corresponding T1-weighted MRI image. *Left*: pre-contrast enhanced MRI. *Right*: post-contrast enhanced MRI. *Bottom row*: fused PET/MRI image. Reprinted with permission from Judenhofer et al. [40]

properties. Multi-modal contrast agents and imaging probes under development will help solve this problem [87]. Despite the great wealth of information that such probes provide, their development is far from trivial, representing an important challenge to synthetic chemists [88]. An example of a multimodal probe based on a MRI active nanoparticle is shown in Fig. 15.27.

These probes may be made sensitive to other modalities, such as optical, by attaching the appropriate molecule to the nanoparticle. Disease processes often can be identified by altered molecular profiles and/or cell behavior before to anatomic alterations can be visualized. The more we learn in this regard, the more this seems

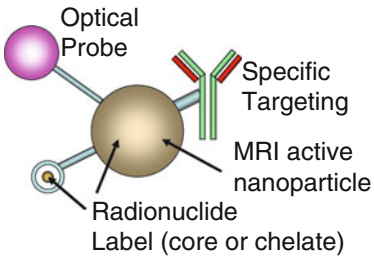

Fig. 15.27 Multimodal nanoparticle suitable for simultaneous PET and MRI imaging

to be a general phenomenon. Insight into these processes could potentially allow (1) the early detection of disease, (2) more accurate prognoses and personalized treatments, (3) the ability to monitor the effectiveness of therapeutic treatments, and, (4) improvements in our understanding of how cells behave and interact in their intact environment in living subjects. Molecular imaging with PEt already has profoundly affected our understanding in preclinical and clinical areas including cancer research and many aspects of neuroscience. MRI is in its early stages of moving from structural and functional imaging to molecular imaging, but this and requires considerable development. The combined use of PET and MRI with these proposed multi-modality imaging agents could be extraordinarily valuable in advancing our understanding of cellular pathophysiology.

Nanoparticles may not only provide sensitive and specific imaging information in cancer patients, but also selectively deliver anticancer drugs to tumor sites [89–91]. There are examples of using nanoparticles as drug delivery agents [92, 93]; more recently, magnetically guided nanoparticles have been used to deliver therapeutic drugs to the specific areas [94]. Although the feasibility of using targeted magnetic iron oxide nanoparticles (MINO) for tumor imaging and therapy is demonstrated, methods and strategies to produce tumor targeted imaging probes with a high specificity and sensitivity still are greatly needed [95, 96]. The added benefit of using nanoparticles for therapy requires that the therapeutic drug stays attached to the nanoparticle until it reaches the desired site. After two decades of effort, iron oxide nanoparticles have become a powerful platform, but are not yet in widespread use clinically [96]. There are questions about how to optimize the nanoparticle-therapeutic drug constructs for delivering the drug to the tumor site and how magnetic direction might be optimized for delivery using magnetically directed drug constructs. By combining the MRI visualization of these nanoparticles with the ability to quantify the concentration of the nanoparticles with PET, we have a powerful tool for investigating the fate of these nanoparticles. Labeling the therapeutic drug with a PET tracer and following the uptake of the nanoparticle with MRI, allows us to visualize clearly the fate of the drug versus that of the nanoparticle as they dissociate in vivo. It will be possible to label a magnetically active nanoparticle in the core and observe the loss in signal as the nanoparticle changes its magnetic properties over time in vivo, while concurrently tracking the total number and

distribution of iron atoms from the nanoparticles using the PET signal, which remains sensitive to the iron regardless of its chemical form.

Various biological molecules attached to nanoparticles have been used in vitro and in vivo. To date, studies showed that the polymer-coated nanoparticles have minimal impact on cell viability and function. Examples include:

- Monoclonal Antibodies. Two initial approaches were to conjugate dextran-coated particles to internalizing monoclonal antibodies and the HIV-tat-peptide. In the first case, the particles end up in the cell in small vesicles or endosomes, and, in the second case in the nucleus.
- Stem Cells. Using stem cells as delivery vehicles opens up the opportunity for targeting therapeutic proteins to the damaged or degenerating central nervous system. Most cellular imaging studies to date were conducted in disease models of the central nervous system (CNS); recently, the infarcted heart received attention.
- Cell Migration and Cell Trafficking. There are several examples of MRI imaging of cell migration following transplantation in the CNS.
- Transfection Agents. Another interesting area is employing iron-oxide nanoparticles coated with a transfection agent (TA). TAs usually are positively charged, bind rapidly to negatively charged cell membranes, and can shuttle associated macromolecules (i.e., oligonucleotides) into cells. The same concept applies for the intracellular delivery of SPIO particles.

We will be able to quantitatively map the dynamics of these molecular imaging probes, and measure their final concentrations. There is a difference in scale of the two types of imaging agents. Iron-based MRI contrast agents usually require about 50–100 μmol of iron per kilogram of body weight to give good semi-quantitative images, while PET tracers usually need about 1 nmol of tracer per kilogram of body weight. By using the two in conjunction, we gain the sensitivity and quantitation of the PET tracer, while using the anatomical sensitivity of the MRI agent to obtain their precise location and volume so that the PET images can be corrected for partial-volume effects in small structures.

6 Summary

The instruments and applications of PET combined with MRI are just beginning to scratch the surface of what is achievable with multi-modality imaging. The ability to view a metabolic or physiological process from several vantage points simultaneously gives us a new perspective in understanding nature. We believe PET/MRI is a cornerstone of these new developments. Even more modalities, such as optical, and ultrasound techniques might well be combined with PET/MRI, and undoubtedly will be valuable research tools for pre-clinical human and small-animal research in the near future.

Acknowledgments This work was supported by the U.S. Department of Energy (OBER) under Prime Contract No. DE-AC02-98CH10886.

References

1. Shokeen M, Fettig NM, Rossin R (2008) Synthesis, in vitro and in vivo evaluation of radiolabeled nanoparticles. Q J Nucl Med Mol Imaging 52:267–77.
2. Townsend DW, Cherry SR (2001) Combining anatomy and function: the path to true image fusion. Eur Radiol 11:1968–74.
3. Yamamoto S, Kuroda K, Senda M (2003) Scintillator selection for MR-compatible gamma detectors. Nuclear Science, IEEE Transactions on 50:1683–1685.
4. Christensen NL, Hammer BE, Heil BG, Fetterly K (1995) Positron emission tomography within a magnetic field using photomultiplier tubes and lightguides. Phys Med Biol 40:691–7.
5. Lucas AJ, Hawkes RC, Ansorge RE, Williams GB, Nutt RE, Clark JC, et al. (2006) Development of a combined microPET-MR system. Technol Cancer Res Treat 5:337–41.
6. Marsden PK, Strul D, Keevil SF, Williams SC, Cash D (2002) Simultaneous PET and NMR. Br J Radiol 75 Spec No:S53-9.
7. Shao Y, Cherry SR, Farahani K, Meadors K, Siegel S, Silverman RW, et al. (1997) Simultaneous PET and MR imaging. Phys Med Biol 42:1965–70.
8. Shao Y, Cherry SR, Farahani K, Slates R, Silverman RW, Meadors K, et al. (1997) Development of a PET detector system compatible with MRI/NMR systems. Nuclear Science, IEEE Transactions on 44:1167–1171.
9. Slates R, Cherry S, Boutefnouchet A, Yiping S, Dahlborn M, Farahani K (1999) Design of a small animal MR compatible PET scanner. Nuclear Science, IEEE Transactions on 46:565–570.
10. Catana C, Procissi D, Wu Y, Judenhofer MS, Qi J, Pichler BJ, et al. (2008) Simultaneous in vivo positron emission tomography and magnetic resonance imaging. Proc Natl Acad Sci U S A 105:3705–10.
11. Catana C, Wu Y, Judenhofer MS, Qi J, Pichler BJ, Cherry SR (2006) Simultaneous acquisition of multislice PET and MR images: initial results with a MR-compatible PET scanner. J Nucl Med 47:1968–76.
12. Pichler BJ, Judenhofer MS, Catana C, Walton JH, Kneilling M, Nutt RE, et al. (2006) Performance test of an LSO-APD detector in a 7-T MRI scanner for simultaneous PET/MRI. J Nucl Med 47:639–47.
13. Pichler BJ, Judenhofer MS, Wehrl HF (2008) PET/MRI hybrid imaging: devices and initial results. Eur Radiol 18:1077–86.
14. Schlyer D, Rooney W, Woody C, Vaska P, Kriplani A, Stoll S (2004) Development of a simultaneous PET/MRI scanner. Nuclear Science Symposium Conference Record, 2004 IEEE, vol. 6, pp. 3419–3421 Vol. 6.
15. Judenhofer MS, Catana C, Swann BK, Siegel SB, Jung WI, Nutt RE, et al. (2007) PET/MR images acquired with a compact MR-compatible PET detector in a 7-T magnet. Radiology 244:807–14.
16. Woody C, Schlyer D, Vaska P, Tomasi D, Solis-Najera S, Rooney W, et al. (2007) Preliminary studies of a simultaneous PET/MRI scanner based on the RatCAP small animal tomograph. Nuclear Instruments and Methods in Physics Research Section A: Accelerators, Spectrometers, Detectors and Associated Equipment 571:102–105.
17. Junnarkar SS, Fried J, O'Connor P, Radeka V, Vaska P, Purschke M, et al. (2006) MRI Compatible G-Link and PCI Based Data Acquisition Hardware for the RatCAP Scanner. Nuclear Science Symposium Conference Record, 2006. IEEE, vol. 1, pp. 380–383.
18. Cutler PD, Cherry SR, Hoffman EJ, Digby WM, Phelps ME (1992) Design features and performance of a PET system for animal research. J Nucl Med 33:595–604.
19. Hammer BE. NMR-PET scanner apparatus US Patent Number 4,939, 464. 1990.
20. Moses WW, Derenzo SE, Budinger TF (1994) PET detector modules based on novel detector technologies. Nuclear Instruments and Methods in Physics Research Section A: Accelerators, Spectrometers, Detectors and Associated Equipment 353:189–194.

21. Cherry SR, Shao Y, Siegel S, Silverman RW, Mumcuoglu E, Meadors K, et al. (1995) Optical fiber readout of scintillator arrays using a multi-channelPMT: a high resolution PET detector for animal imaging. vol. 3, pp.
22. Cherry SR, Shao Y, Tornai MP, Siegel S, Ricci AR, Phelps ME (1995) Collection of scintillation light from small BGO crystals. IEEE Transactions on Nuclear Science 42:1058–1063.
23. Garlick PB, Marsden PK, Cave AC, Parkes HG, Slates R, Shao Y, et al. (1997) PET and NMR dual acquisition (PANDA): applications to isolated, perfused rat hearts. NMR Biomed 10:138–42.
24. Slates RB, Farahani K, Shao Y, Marsden PK, Taylor J, Summers PE, et al. (1999) A study of artefacts in simultaneous PET and MR imaging using a prototype MR compatible PET scanner. Phys Med Biol 44:2015–27.
25. Lecomte R, Schmitt D, Lightstone AW, McIntyre RJ (1985) Performance characteristics of BGO-silicon avalanche photodiode detectors for PET. IEEE Transactions on Nuclear Science 32:482–486.
26. Petrillo GA, McIntyre RJ, Lecomte R, Lamoureux G, Schmitt D (1984) Scintillation detection with large-area reach-through avalanche photodiodes. IEEE Transactions on Nuclear Science 31:417–423.
27. Lecomte R, Martel C, Carrier C (1989) Status of BGO-avalanche photodiode detectors for spectroscopic and timing measurements. Nucl. Instrum. Meth. Phys. Res 278:585–597.
28. Lecomte R, Cadorette J, Jouan A, Heon M, Rouleau D, Gauthier G (1990) High resolution positron emission tomography with a prototypecamera based on solid state scintillation detectors. IEEE Transactions on Nuclear Science 37:805–811.
29. Lecomte R, Cadorette J, Rodrigue S, Lapointe D, Rouleau D, Bentourkia M, et al. (1996) Initial results from the Sherbrooke avalanche photodiode positron tomograph. Nuclear Science, IEEE Transactions on 43:1952–1957.
30. Fontaine R, Belanger F, Viscogliosi N, Semmaoui H, Tetrault MA, Michaud JB, et al. (2005) The architecture of LabPET/spl trade/, a small animal APD-based digital PET scanner. Nuclear Science Symposium Conference Record, 2005 IEEE, vol. 5, pp. 2785–2789.
31. Bergeron M, Cadorette J, Beaudoin JF, Lepage MD, Robert G, Selivanov V, et al. (2009) Performance Evaluation of the LabPET APD-Based Digital PET Scanner. Nuclear Science, IEEE Transactions on 56:10–16.
32. Schmelz C, Bradbury SM, Holl I, Lorenz E, Renker D, Ziegler S (1995) Feasibility study of an avalanche photodiode readout for a highresolution PET with nsec time resolution. IEEE Transactions on Nuclear Science 42:1080–1084.
33. Casey ME, Dautet H, Waechter D, Lecomte R, Eriksson L, Schmand M, et al. (1998) An LSO block detector for PET using an avalanche photodiode array. vol. 2, pp.
34. Pichler BJ, Swann BK, Rochelle J, Nutt RE, Cherry SR, Siegel SB (2004) Lutetium oxyorthosilicate block detector readout by avalanche photodiode arrays for high resolution animal PET. Phys Med Biol 49:4305–19.
35. Pichler B, Boning C, Lorenz E, Mirzoyan R, Pimpl W, Schwaiger M, et al. (1998) Studies with a prototype high resolution PET scanner based onLSO-APD modules. IEEE Transactions on Nuclear Science 45:1298–1302.
36. Binkley DM, Puckett BS, Casey ME, Lecomte R, Saoudi A (1999) A power efficient, low noise, wideband, integrated CMOSpreamplifier for LSO/APD PET systems. vol. 1, pp.
37. Lecomte R, Pepin CM, Lepage MD, Pratte JF, Dautet H, Binkley DM (2001) Performance analysis of phoswich/APD detectors and low-noise CMOSpreamplifiers for high-resolution PET systems. IEEE Transactions on Nuclear Science 48:650–655.
38. Pichler B, Lorenz E, Mirzoyan R, Pimpl W, Roder F, Schwaiger M, et al. (1997) Performance test of a LSO-APD PET module in a 9.4 Tesla magnet. Nuclear Science Symposium, 1997. IEEE, vol. 2, pp. 1237–1239 vol.2.
39. Schlyer D, Vaska P, Tomasi D, Woody C, Maramraju SH, Southekal S, et al. (2007) A Simultaneous PET/MRI scanner based on RatCAP in small animals. Nuclear Science Symposium Conference Record, 2007. NSS '07. IEEE, vol. 5, pp. 3256–3259.

40. Judenhofer MS, Wehrl HF, Newport DF, Catana C, Siegel SB, Becker M, et al. (2008) Simultaneous PET-MRI: a new approach for functional and morphological imaging. Nat Med 14:459–65.
41. Pratte JF, Junnarkar S, Deptuch G, Fried J, O'Connor P, Radeka V, et al. (2008) The RatCAP Front-End ASIC. Nuclear Science, IEEE Transactions on 55:2727–2735.
42. Junnarkar SS, Fried J, Southekal S, Pratte JF, O'Connor P, Radeka V, et al. (2008) Next Generation of Real Time Data Acquisition, Calibration and Control System for the RatCAP Scanner. Nuclear Science, IEEE Transactions on 55:220–224.
43. Maramraju SH, Junnarkar S, Ravindranath B, Southekal S, Stoll S, Smith SD, et al. (2008) An MR compatible PET scanner based on RatCAP for small animal imaging at 9.4T. Nuclear Science Symposium Conference Record, 2008. NSS '08. IEEE, pp. 3679–3682.
44. Karplus E, Farrell R, Shah K. Position sensitive solid state detector with internal gain. US patent No : 6,998,619 B2. 2004.
45. Shah KS, Grazioso R, Farrell R, Glodo J, McClish M, Entine G, et al. (2004) Position sensitive APDs for small animal PET imaging. IEEE Transactions on Nuclear Science 51:91–95.
46. Burr KC, Ivan A, LeBlanc J, Zelakiewicz S, McDaniel DL, Kim CL, et al. (2003) Evaluation of a position sensitive avalanche photodiode for PET. Nuclear Science, IEEE Transactions on 50:792–796.
47. Levin CS, Foudray AMK, Olcott PD, Habte F (2004) Investigation of position sensitive avalanche photodiodes for a new high-resolution PET detector design. Nuclear Science, IEEE Transactions on 51:805–810.
48. Yang Y, Wu Y, Qi J, St James S, Du H, Dokhale PA, et al. (2008) A prototype PET scanner with DOI-encoding detectors. Journal of Nuclear Medicine 49:1132.
49. Burr KC, Ivan A, Castleberry DE, LeBlanc JW, Shah KS, Farrell R, et al. (2004) Evaluation of a prototype small-animal PET detector with depth-of-interaction encoding. IEEE Transactions on Nuclear Science 51:1791–1798.
50. Dokhale PA, Silverman RW, Shah KS, Grazioso R, Farrell R, Glodo J, et al. (2004) Performance measurements of a depth-encoding PET detector module based on position-sensitive avalanche photodiode read-out. Physics in Medicine and Biology 49:4293–4304.
51. Yang Y, Dokhale PA, Silverman RW, Shah KS, McClish MA, Farrell R, et al. (2006) Depth of interaction resolution measurements for a high resolution PET detector using position sensitive avalanche photodiodes. Physics in Medicine and Biology 51:2131–2142.
52. Saveliev V, Golovin V (2000) Silicon avalanche photodiodes on the base of metal-resistor-semiconductor (MRS) structures. Nuclear Instruments and Methods in Physics Research Section A: Accelerators, Spectrometers, Detectors and Associated Equipment 442:223–229.
53. Otte AN, Barral J, Dolgoshein B, Hose J, Klemin S, Lorenz E, et al. (2005) A test of silicon photomultipliers as readout for PET. Nuclear Instruments and Methods in Physics Research Section A: Accelerators, Spectrometers, Detectors and Associated Equipment 545:705–715.
54. Llosa G, Belcari N, Bisogni MG, Collazuol G, Del Guerra A, Marcatili S, et al. (2008) Evaluation of the first Silicon Photomultiplier matrices for a small animal PET scanner. Nuclear Science Symposium Conference Record, 2008. NSS '08. IEEE, pp. 3574–3580.
55. Llosa G, Belcari N, Bisogni MG, Collazuol G, Marcatili S, Moehrs S, et al. (2009) Energy and Timing Resolution Studies With Silicon Photomultipliers (SiPMs) and 4-Pixel SiPM Matrices for PET. Nuclear Science, IEEE Transactions on 56:543–548.
56. Herbert DJ, Saveliev V, Belcari N, D'Ascenzo N, Del Guerra A, Golovin A (2006) First results of scintillator readout with silicon photomultiplier. Nuclear Science, IEEE Transactions on 53:389–394.
57. Lucas AJ, Hawkes RC, Guerra P, Ansorge RE, Nutt RE, Clark JC, et al. (2006) Development of a combined microPETÂ®-MR system. Nuclear Science Symposium Conference Record, 2006. IEEE, vol. 4, pp. 2345–2348.
58. Gilbert K, Handler W, Scholl T, Odegaard J, Chronik B (2006) Design of field-cycled magnetic resonance systems for small animal imaging. Physics in Medicine and Biology 51:2825–2842.

59. Gilbert KM, Scholl TJ, Handler WB, Alford JK, Chronik BA (2009) Evaluation of a positron emission tomography (PET)-compatible field-cycled MRI (FCMRI) scanner. Magn Reson Med.
60. Slates R, Shao Y, Farahani K, Marsden PK, Cherry SR, Meadors K, et al. (1997) Assessment of artifacts in simultaneous PET and MR imaging. Nuclear Science Symposium, 1997. IEEE, vol. 2, pp. 1357–1360 vol.2.
61. Zhang Z, Olcott PD, Levin CS (2007) A New Positioning Algorithm for Position-Sensitive Avalanche Photodiodes. Nuclear Science, IEEE Transactions on 54:433–437.
62. Chaudhari AJ, Joshi AA, Yibao W, Leahy RM, Cherry SR, Badawi RD (2008) Spatial distortion correction and crystal identification for position-sensitive avalanche photodiode-based PET scanners. Nuclear Science Symposium Conference Record, 2008. NSS '08. IEEE, pp. 5045–5052.
63. Chaudhari AJ, Joshi AA, Yibao W, Leahy RM, Cherry SR, Badawi RD (2009) Spatial Distortion Correction and Crystal Identification for MRI-Compatible Position-Sensitive Avalanche Photodiode-Based PET Scanners. Nuclear Science, IEEE Transactions on 56:549–556.
64. Zhang J, Foudray AMK, Olcott PD, Farrell R, Shah K, Levin CS (2007) Performance Characterization of a Novel Thin Position-Sensitive Avalanche Photodiode for 1 mm Resolution Positron Emission Tomography. Nuclear Science, IEEE Transactions on 54:415–421.
65. Raylman RR, Hammer BE, Christensen NL (1996) Combined MRI-PET scanner: a Monte Carlo evaluation of the improvements in PET resolution due to the effects of a static homogeneous magnetic field. Nuclear Science, IEEE Transactions on 43:2406–2412.
66. Hammer BE, Christensen NL (1995) Measurement of positron range in matter in strong magnetic fields. Nuclear Science, IEEE Transactions on 42:1371–1376.
67. Hammer BE, Christensen NL, Heil BG (1994) Use of a magnetic field to increase the spatial resolution of positron emission tomography. Med Phys 21:1917–20.
68. Wirrwar A, Vosberg H, Herzog H, Halling H, Weber S, Muller-Gartner HW (1997) 4.5 tesla magnetic field reduces range of high-energy positrons-potential implications for positron emission tomography. Nuclear Science, IEEE Transactions on 44:184–189.
69. Zaidi H, Hasegawa B (2003) Determination of the attenuation map in emission tomography. J Nucl Med 44:291–315.
70. Zaidi H, Montandon ML, Slosman DO (2003) Magnetic resonance imaging-guided attenuation and scatter corrections in three-dimensional brain positron emission tomography. Med Phys 30:937–48.
71. Rowell NP, Glaholm J, Flower MA, Cronin B, McCready VR (1992) Anatomically derived attenuation coefficients for use in quantitative single photon emission tomography studies of the thorax. Eur J Nucl Med 19:36–40.
72. Zaidi H (2007) Is MR-guided attenuation correction a viable option for dual-modality PET/MR imaging? Radiology 244:639–42.
73. Hofmann M, Pichler B, Scholkopf B, Beyer T (2009) Towards quantitative PET/MRI: a review of MR-based attenuation correction techniques. Eur J Nucl Med Mol Imaging 36 Suppl 1:S93–104.
74. Beyer T, Weigert M, Quick HH, Pietrzyk U, Vogt F, Palm C, et al. (2008) MR-based attenuation correction for torso-PET/MR imaging: pitfalls in mapping MR to CT data. Eur J Nucl Med Mol Imaging 35:1142–6.
75. Day SE, Kettunen MI, Gallagher FA, Hu DE, Lerche M, Wolber J, et al. (2007) Detecting tumor response to treatment using hyperpolarized 13C magnetic resonance imaging and spectroscopy. Nat Med 13:1382–7.
76. Thompson JK, Peterson MR, Freeman RD (2003) Single-neuron activity and tissue oxygenation in the cerebral cortex. Science 299:1070–2.
77. Belliveau JW, Cohen MS, Weisskoff RM, Buchbinder BR, Rosen BR (1991) Functional studies of the human brain using high-speed magnetic resonance imaging. J Neuroimaging 1:36–41.
78. Mountz JM (2007) Nuclear medicine in the rehabilitative treatment evaluation in stroke recovery. Role of diaschisis resolution and cerebral reorganization. Eura Medicophys 43:221–39.
79. van Eijsden P, Hyder F, Rothman DL, Shulman RG (2009) Neurophysiology of functional imaging. Neuroimage 45:1047–54.

80. Gerstl F, Windischberger C, Mitterhauser M, Wadsak W, Holik A, Kletter K, et al. (2008) Multimodal imaging of human early visual cortex by combining functional and molecular measurements with fMRI and PET. Neuroimage 41:204–11.
81. Stadlbauer A, Polking E, Prante O, Nimsky C, Buchfelder M, Kuwert T, et al. (2009) Detection of tumour invasion into the pyramidal tract in glioma patients with sensorimotor deficits by correlation of (18)F-fluoroethyl-L: -tyrosine PET and magnetic resonance diffusion tensor imaging. Acta Neurochir (Wien) 151:1061–9.
82. Sobesky J, Zaro Weber O, Lehnhardt FG, Hesselmann V, Neveling M, Jacobs A, et al. (2005) Does the mismatch match the penumbra? Magnetic resonance imaging and positron emission tomography in early ischemic stroke. Stroke 36:980–5.
83. Wolf RL, Detre JA (2007) Clinical neuroimaging using arterial spin-labeled perfusion magnetic resonance imaging. Neurotherapeutics 4:346–59.
84. Wissmeyer M, Altrichter S, Pereira VM, Viallon M, Federspiel A, Seeck M, et al. (2009) Arterial spin-labeling MRI perfusion in tuberous sclerosis: Correlation with PET. J Neuroradiol.
85. Chen JJ, Wieckowska M, Meyer E, Pike GB (2008) Cerebral Blood Flow Measurement Using fMRI and PET: A Cross-Validation Study. Int J Biomed Imaging 2008:516359.
86. Jack CR, Jr., Lowe VJ, Senjem ML, Weigand SD, Kemp BJ, Shiung MM, et al. (2008) 11C PiB and structural MRI provide complementary information in imaging of Alzheimer's disease and amnestic mild cognitive impairment. Brain 131:665–80.
87. Jennings LE, Long NJ (2009) 'Two is better than one'--probes for dual-modality molecular imaging. Chem Commun (Camb):3511–24.
88. Cheon J, Lee JH (2008) Synergistically integrated nanoparticles as multimodal probes for nanobiotechnology. Acc Chem Res 41:1630–40.
89. Gupta AK, Naregalkar RR, Vaidya VD, Gupta M (2007) Recent advances on surface engineering of magnetic iron oxide nanoparticles and their biomedical applications. Nanomed 2:23–39.
90. Hanessian S, Grzyb JA, Cengelli F, Juillerat-Jeanneret L (2008) Synthesis of chemically functionalized superparamagnetic nanoparticles as delivery vectors for chemotherapeutic drugs. Bioorg Med Chem 16:2921–31.
91. Yang CH, Huang KS, Lin YS, Lu K, Tzeng CC, Wang EC, et al. (2009) Microfluidic assisted synthesis of multi-functional polycaprolactone microcapsules: incorporation of CdTe quantum dots, Fe3O4 superparamagnetic nanoparticles and tamoxifen anticancer drugs. Lab Chip 9:961–5.
92. Peng XH, Qian X, Mao H, Wang AY, Chen ZG, Nie S, et al. (2008) Targeted magnetic iron oxide nanoparticles for tumor imaging and therapy. Int J Nanomedicine 3:311–21.
93. Murakami T, Tsuchida K (2008) Recent advances in inorganic nanoparticle-based drug delivery systems. Mini Rev Med Chem 8:175–83.
94. Barry SE (2008) Challenges in the development of magnetic particles for therapeutic applications. Int J Hyperthermia 24:451–66.
95. McCarthy JR, Weissleder R (2008) Multifunctional magnetic nanoparticles for targeted imaging and therapy. Adv Drug Deliv Rev 60:1241–51.
96. Xie J, Huang J, Li X, Sun S, Chen X (2009) Iron oxide nanoparticle platform for biomedical applications. Curr Med Chem 16:1278–94.